Shen, Fuhui; Münstermann, Sebastian; Lian, Junhe

A unified fracture criterion considering stress state dependent transition of failure mechanisms in bcc steels at -196 °c

Published in:
International Journal of Plasticity

DOI:
10.1016/j.ijplas.2022.103365

Published: 01/09/2022

Document Version
Publisher's PDF, also known as Version of record

Please cite the original version:
Shen, F., Münstermann, S., & Lian, J. (2022). A unified fracture criterion considering stress state dependent transition of failure mechanisms in bcc steels at -196 °c. *International Journal of Plasticity*, *156*, Article 103365. https://doi.org/10.1016/j.ijplas.2022.103365

International Journal of Plasticity 156 (2022) 103365

Contents lists available at ScienceDirect

International Journal of Plasticity

journal homepage: www.elsevier.com/locate/ijplas

A unified fracture criterion considering stress state dependent transition of failure mechanisms in bcc steels at –196 °C

Fuhui Shen [a,b], Sebastian Münstermann [a], Junhe Lian [b,*]

[a] Integrity of Materials and Structures, Steel Institute, RWTH Aachen University, Intzestraβe 1, Aachen 52072, Germany
[b] Advanced Manufacturing and Materials, Department of Mechanical Engineering, Aalto University, Puumiehenkuja 3, Espoo 02150, Finland

ARTICLE INFO

Keywords:
Stress states
Fracture criterion
Cleavage fracture
Shear fracture
Threshold triaxiality

ABSTRACT

The fracture properties of a high-strength steel with a body-centered cubic (bcc) crystal structure have been characterized at –196 °C by performing tensile tests with different specimen geometries, three-point bending tests using Charpy specimens, and fracture mechanics tests, covering a broad range of stress states under quasi-static conditions. Both strength and ductility of the bcc steel are significantly increased when the temperature is decreased from room temperature to –196 °C. Enormous plasticity occurs in the material during tensile tests using various specimens at –196 °C, while macroscopic brittle fracture takes place in high triaxiality scenarios. A stress state dependence of ductile to brittle transition properties is observed, as the failure mechanisms at –196 °C change from cleavage fracture to shear failure with decreasing stress triaxiality. A unified stress-state-dependent fracture criterion, which considers the transition of failure mechanisms, is proposed to describe the fracture properties of similar bcc materials at cryogenic temperatures. The threshold triaxiality at which the transition of failure mechanisms takes place is a material property that is determined by the strain hardening capacity and fracture strength. In addition, a probabilistic formulation relying on the extreme value distribution has been incorporated into the model to render the statistical nature of cleavage fracture.

1. Introduction

With the recent exciting cryogenic applications in aerospace and energy transportation fields, the mechanical performance of engineering materials operating at cryogenic temperatures has become a demanding feature, leading to the development of several high/medium entropy alloys with a face-centered cubic (fcc) structure (Gludovatz et al., 2014; Sathiyamoorthi et al., 2019; Sun et al., 2018). For metallic materials, especially steels, this operating temperature is usually not an option for body-centered cubic (bcc) crystal structures, as they typically exhibit sudden brittle fracture without any plastic deformation (Anderson, 2017). However, lately, extraordinary ductility and high toughness at cryogenic temperatures, such as liquid nitrogen temperature (−196 °C), were reported in some bcc metallic structures including nanostructured metals (Wang et al., 2004) and an ultra-fine grained steel (Kimura et al., 2008) due to the ultra-fine grain structure and the dispersion of nano-sized particles. Although these findings have been only limited to lab materials with very specific alloys or ultra-fine nano-scale microstructures, they substantially motivate research to further explore the fracture behavior of modern high-strength steels under cryogenic temperatures.

For conventional bcc metals with ordinary cleavage and brittle fracture, fracture mechanics tests using thick specimens with a

* Corresponding author.
E-mail address: junhe.lian@aalto.fi (J. Lian).

https://doi.org/10.1016/j.ijplas.2022.103365
Received 20 March 2022; Received in revised form 25 May 2022;
Available online 26 June 2022

sharp pre-crack seem enough to conservatively evaluate the cryogenic fracture properties under plane-strain tension with significantly large hydrostatic pressure. However, when the cleavage fracture with enormous plasticity is considered, questions are raised concerning the completeness of the stress state characterization. As reported in the last two decades, the influence of stress states on ductile fracture has been shown significant for various engineering materials (Bai and Wierzbicki, 2010; Brünig et al., 2018; Habib et al., 2019; Khan and Liu, 2012b; Li and Fang, 2022; Li et al., 2018; Lian et al., 2013; Lou et al., 2017; Lou and Yoon, 2017; Mohr and Marcadet, 2015; Mu et al., 2020; Peng et al., 2021; Quach et al., 2020; Thomas et al., 2016; Torki et al., 2021; Xue, 2007; Xue and Wierzbicki, 2008). The effects of stress states, particularly across a large range of stress triaxiality and Lode angle, on the cleavage fracture of high-strength materials have not attracted sufficient research attention, as the typical fracture mechanics tests only consider a narrow and specific range of stress states, i.e., high stress triaxiality with more or less constant Lode angle parameter (Anderson, 2017; Pineau et al., 2016). Therefore, for a comprehensive evaluation of the fracture performance of materials at cryogenic temperatures, a much more comprehensive range of stress states shall be involved.

The cleavage fracture can be generally described as a sequence of nucleation of a microcrack and the propagation of the crack by overcoming several barriers to reach a sufficient length, which leads to the final failure of the component (Chen and Cao, 2014; Pineau et al., 2016). Recognizing the detriment of crack propagation, Orowan (1949) stressed that the local maximum principal stress plays an essential role in the cleavage fracture propagation, and its critical value, as a material constant, could be referred to as the cleavage fracture strength. Assuming a pre-existing flaw in the material, both fracture mechanics theory as *a global approach* and several physics-informed models belonging to the *local approach* to fracture, have been quite successful in deriving a relatively conservative assessment of the cleavage fracture toughness (Anderson, 2017; Knott, 2015; Pineau et al., 2016). However, the new cleavage fracture behavior coupled with enormous plasticity has raised challenges to the existing models. For the global approach, it is challenging to incorporate enormous plasticity by nature. Certain efforts have been made during the past years to include plasticity in the local approach models (Gao et al., 2006; He et al., 2017; Ruggieri and Dodds, 2017), which are still intrinsically based on the cleavage fracture strength theory and focused only on the influence of plastic deformation on the cleavage fracture strength. This strategy could work with cleavage fracture with local limited plastic deformation, such as the plastic deformation right at the crack tip; however, it would be challenged by the enormous plasticity of the newly discovered cleavage fracture behavior. In addition, several models have also been developed to consider the effects of stress state and constraints on the cleavage fracture properties (Boåsen et al., 2019; Neimitz and Dzioba, 2015; Testa et al., 2020). However, more challenges are brought in understanding and predicting the observed change of failure mechanisms over stress states at cryogenic temperatures with existing models.

On the other hand, fracture properties of metallic materials after significant plastic deformation can be described using damage mechanics models, which have gained substantial development (Benzerga et al., 2016; Besson, 2009; Lemaitre, 2012; Pineau et al., 2016; Tekkaya et al., 2020). One great success these models achieved is the ability to interpret the influence of stress states on the ductile fracture in a generalized way. Many studies, with only a few selected, showed the fracture behavior with significant plastic deformation over a wider range of stress states could be described in the damage mechanics approach by using initially crack-free specimens with different geometries, such as notched dog-bone, central hole, notched round bar, or cylindrical indentation, etc. (Bai and Wierzbicki, 2008; Khan and Liu, 2012a; Kim et al., 2017; Li et al., 2018; Lian et al., 2019; Papasidero et al., 2015; Roth and Mohr, 2016; Shen et al., 2022). These models seem to be an ideal alternative to simulate the cryogenic fracture with enormous plasticity. However, they also lack the feature to render the sudden cleavage fracture without any plasticity that could still appear at specific stress states.

To fill these scientific gaps induced by the newly discovered cleavage fracture with enormous plasticity in bcc engineering metallic structures, the present study aims to characterize the cryogenic deformation and fracture behavior of a commercially high-strength low-alloyed bainite steel in a much broader range of stress states from negative-triaxiality compression to high-triaxiality tension. This will be the most systematic and comprehensive, in terms of stress states, experimental program that has been applied under liquid nitrogen temperature. Informed by the underlying failure mechanisms under different stress states, a unified fracture criterion is proposed to explain the cryogenic fracture properties of bcc steels, with or without enormous plasticity. By integrating the advantages of damage and fracture mechanics for fracture initiation and propagation, the unified fracture criterion can provide quantitative predictions on the significant variation of plastic deformation due to the transition of failure mechanisms over stress states at the same testing temperature. The calibration and validation of the fracture criterion are elaborated based on experimental results. The observed fracture phenomena and proposed fracture criterion are not exclusive to the investigated material in this study but generally applicable to other similar metallic materials with the bcc crystalline structure, which significantly enriches the current knowledge on fracture properties of metallic materials.

2. Material and experiments

The fracture properties of an X70 pipeline steel with a bcc structure have been investigated under quasi-static conditions at –196 °C over a wide loading spectrum, using flat tensile specimens (2 mm in thickness) with different notch configurations, three-point bending tests using Charpy specimens, and fracture mechanics tests.

2.1. Tensile properties

The anisotropic plasticity of the material was characterized at room temperature (RT) and –196 °C by performing uniaxial tensile tests using smooth dog bone (SDB) specimens according to DIN EN ISO 6892–1. To obtain the tensile properties at –196 °C, specimens were immersed in liquid nitrogen contained in a thermal tank that was attached to a Zwick 1484 machine. A crosshead velocity of 0.4

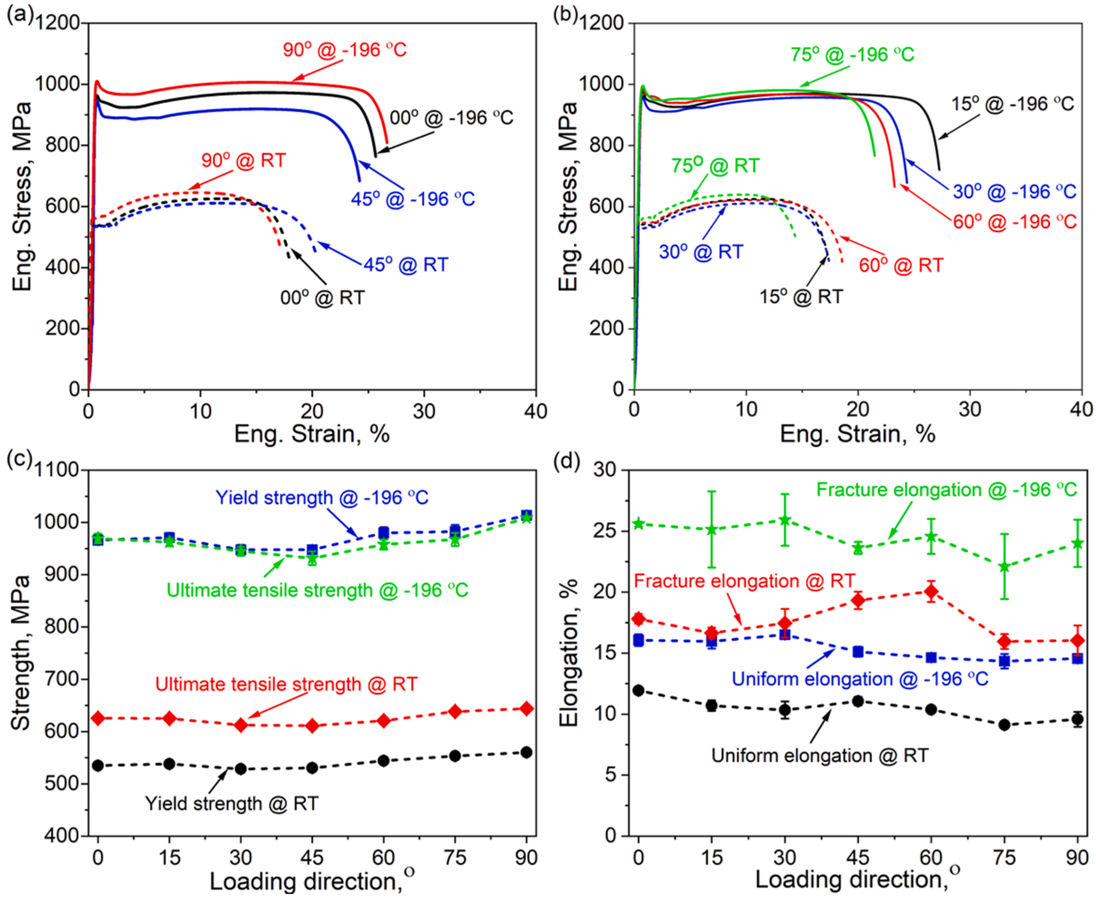

Fig. 1. The orientation-dependent uniaxial tensile properties of the investigated X70 steel at room temperature and –196 °C: Engineering stress vs. strain curves along (a) 0°, 45°, 90°, and (b) 15°, 30°, 60°, 75°; (c) strength anisotropy and (d) elongation anisotropy.

Table 1
Summary of the uniaxial tensile properties at room temperature and –196 °C.

			0°	15°	30°	45°	60°	75°	90°
RT	Yield strength	Mean (MPa)	534.96	538.20	528.37	530.50	544.11	553.15	560.00
		STDEV (MPa)	0.68	3.05	3.59	1.31	2.68	2.74	0.14
	Tensile strength	Mean (MPa)	625.73	624.96	612.33	611.15	620.82	638.30	643.90
		STDEV (MPa)	0.62	1.60	1.37	1.14	2.09	1.43	1.37
	Uniform elongation	Mean (%)	11.94	10.70	10.33	11.06	10.38	9.12	9.58
		STDEV (%)	0.19	0.44	0.70	0.35	0.04	0.25	0.61
	Fracture elongation	Mean (%)	17.81	16.64	17.46	19.33	20.06	15.96	16.04
		STDEV (%)	0.40	0.45	1.18	0.72	0.86	0.61	1.23
–196 °C	Yield strength	Mean (MPa)	966.03	971.20	947.75	947.84	979.96	982.71	1013.69
		STDEV (MPa)	2.09	8.68	9.32	3.56	11.07	12.45	2.70
	Tensile strength	Mean (MPa)	969.18	962.23	944.98	931.63	957.79	967.71	1008.57
		STDEV (MPa)	9.31	7.38	8.68	12.99	9.39	12.46	1.62
	Uniform elongation	Mean (%)	16.06	15.97	16.51	15.12	14.63	14.34	14.56
		STDEV (%)	0.48	0.59	0.22	0.41	0.14	0.59	0.11
	Fracture elongation	Mean (%)	25.58	25.14	25.92	23.63	24.57	22.10	24.01
		STDEV (%)	0.19	3.12	2.12	0.48	1.44	2.67	1.93

mm/min was applied during tensile tests. The engineering stress-strain curves, corresponding to a gage length of 50 mm, along seven different directions are shown in Fig. 1, where apparent anisotropic effects on the plasticity can be observed. The strategy to determine experimental displacements corresponding to a given gage length is explained in the Appendix. The distinct yield stress is identified as the yield strength. The stress and strain corresponding to the maximum load in the post-yielding deformation phase are defined as ultimate tensile strength and uniform elongation, respectively. It is surprisingly noticed that both strength (yield strength and ultimate tensile strength) and ductility (uniform elongation and fracture elongation) are significantly improved in this bcc steel when the

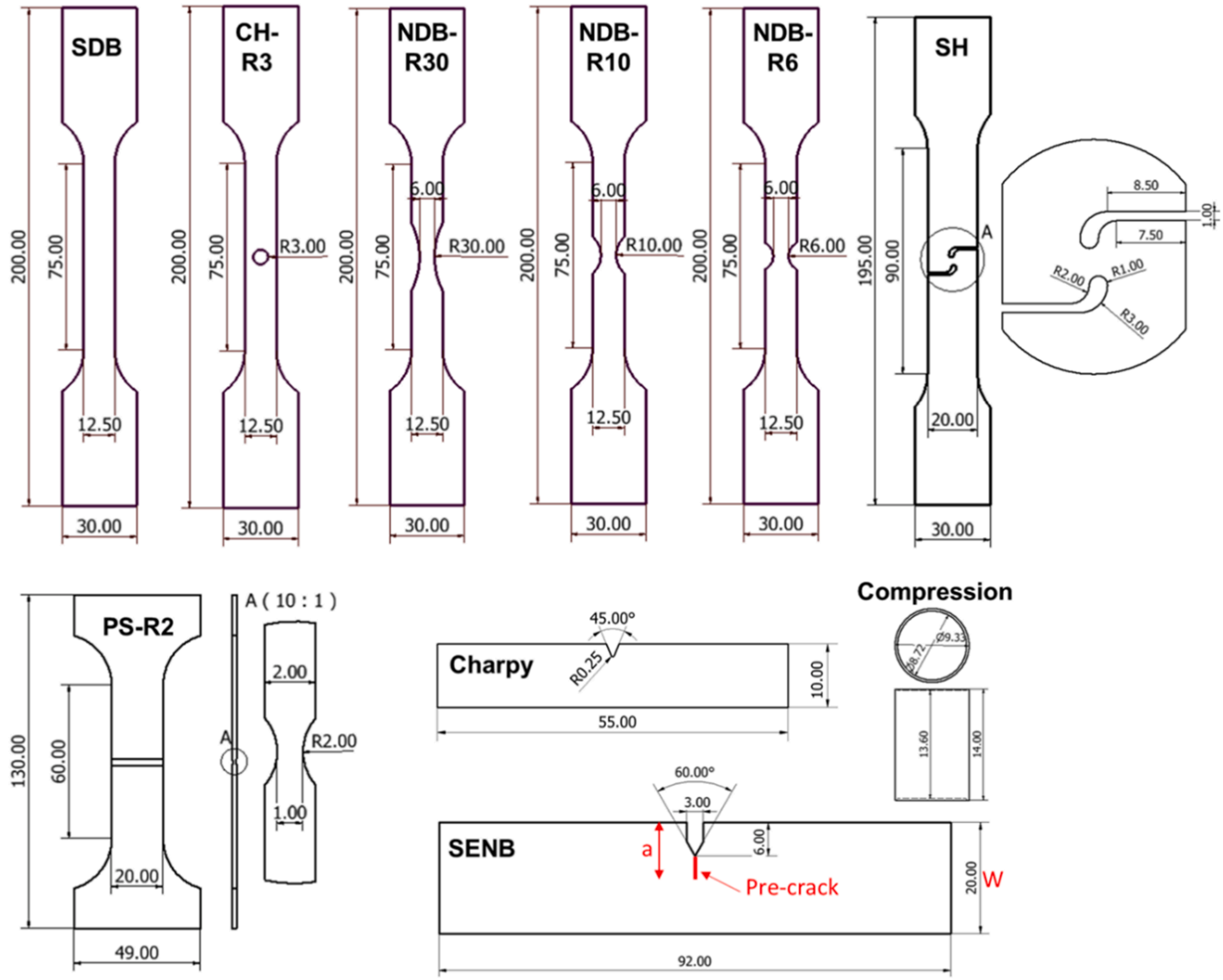

Fig. 2. Dimensions of all specimen geometries used for the plasticity and fracture characterization (all units are mm).

temperature is decreased from RT to –196 °C, which is not expected according to the conventional fracture theories.

Tensile properties obtained from three parallel tests are summarized in Table 1. In addition, the orientation dependence of both yield strength and ultimate tensile strength is similar at both temperatures, as shown in Fig. 1. The previous experimental results of tensile properties of the investigated X70 steel at intermediate temperatures between RT and –150 °C (Shen et al., 2020a) have shown that the anisotropic patterns of strength exhibit negligible temperature dependence, indicating the shape of the yield locus is not affected by temperature. Therefore, the Lankford coefficients of this material are assumed to be independent of temperature, which were measured at RT in the previous publication (Shen et al., 2020b).

2.2. Fracture experiments at –196 °C

The fracture properties along the rolling direction are investigated in this study. Tensile tests were performed at –196 °C using six different flat specimen geometries along the rolling direction. With the adopted shear (SH), central hole (CH), notched dog bone (NDB), and plane strain (PS) specimens, as shown in Fig. 2, the fracture behavior in the stress state range from shear to plane strain tension can be captured in tensile tests. During tensile tests, specimens were immersed in liquid nitrogen, and a crosshead velocity of 0.2 mm/min was applied for these notched specimens. The force-displacement curves of tensile tests from seven parallel experiments at –196 °C are shown in Fig. 3 for four sample geometries. It is also very interesting to observe that a significant amount of plastic deformation occurs at such an extremely low temperature in a high-strength low alloyed steel with a bcc structure, which is not consistent with the frequently reported brittle fracture phenomena in bcc steels. In addition, the very small scatter in fracture displacements, as summarized in Table 2, is also not often observed in cleavage fracture of bcc steels according to the weakest link theory.

The typical brittle fracture without visible plasticity is observed in the quasi-static three-point bending tests using Charpy specimens and fracture mechanics tests using single-edge notched bending (SENB) specimens at –196 °C, as shown in Fig. 3. It is noted that the Charpy tests performed in this study are not in the dynamic mode as regular ones. Instead, a very slow loading velocity of 0.1 mm/

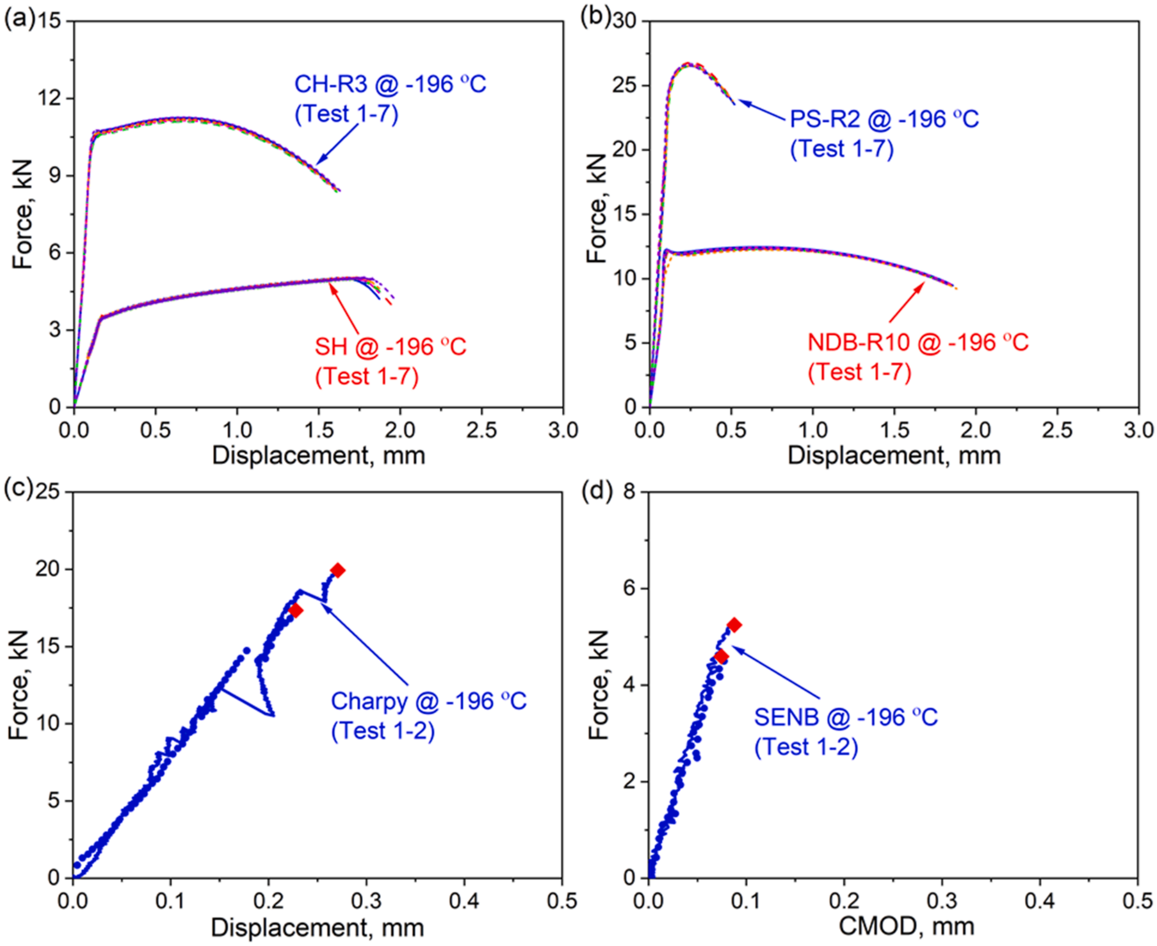

Fig. 3. The experimental force and displacement curves obtained from six different loading conditions at –196 °C.

Table 2
Experimental fracture displacement and force in different specimens tested at –196 °C.

Geometry		#1	#2	#3	#4	#5	#6	#7	Avg.	Dev.
SH	Disp. (mm)	1.65	1.68	1.66	1.73	1.69	1.73	1.77	1.70	0.04
	Force (kN)	5.05	5.05	5.05	5.03	5.06	5.07	5.07	5.05	0.01
CH-R3	Disp. (mm)	1.62	1.47	1.56	1.60	1.59	1.61	1.63	1.58	0.05
	Force (kN)	8.37	9.17	8.70	8.50	8.48	8.38	8.41	8.57	0.27
NDB-R30	Disp. (mm)	2.34	2.36	2.45	2.45	2.51	2.48	2.49	2.46	0.04
	Force (kN)	9.78	9.57	8.99	8.95	9.00	8.85	9.00	9.06	0.22
NDB-R10	Disp. (mm)	1.86	1.82	1.84	1.82	1.86	1.88	1.85	1.85	0.02
	Force (kN)	9.47	9.66	9.45	9.59	9.47	9.22	9.42	9.47	0.13
NDB-R6	Disp. (mm)	1.62	1.64	1.69	1.70	1.71	1.75	1.80	1.70	0.06
	Force (kN)	9.64	9.69	9.33	9.71	9.56	9.44	9.67	9.71	0.40
PS-R2	Disp. (mm)	0.52	0.48	0.50	0.50	0.50	0.51	0.47	0.50	0.02
	Force (kN)	23.53	24.11	23.82	23.82	23.89	23.82	24.08	23.87	0.18
Charpy	Disp. (mm)	0.26	0.23	–	–	–	–	–	0.25	0.02
	Force (kN)	19.94	17.34	–	–	–	–	–	18.64	1.30
SENB	Disp. (mm)	0.09	0.07	–	–	–	–	–	0.08	0.01
	Force (kN)	5.25	4.59	–	–	–	–	–	4.92	0.33

min was applied to the punch in three-point bending tests using both Charpy and SENB specimens to reach a quasi-static condition even for local deformation. The distance between supporting rollers was 40 mm and 82 mm for the Charpy and SENB specimens, respectively. For the creation of a sharp pre-crack, the SENB specimen was subjected to cyclic loading under three-point bending configurations with controlled stress amplitudes. By monitoring the crack development on the polished sample surface, the applied stress amplitude was reduced once the pre-defined crack depth was reached. The depth of a pre-crack in the middle thickness position was

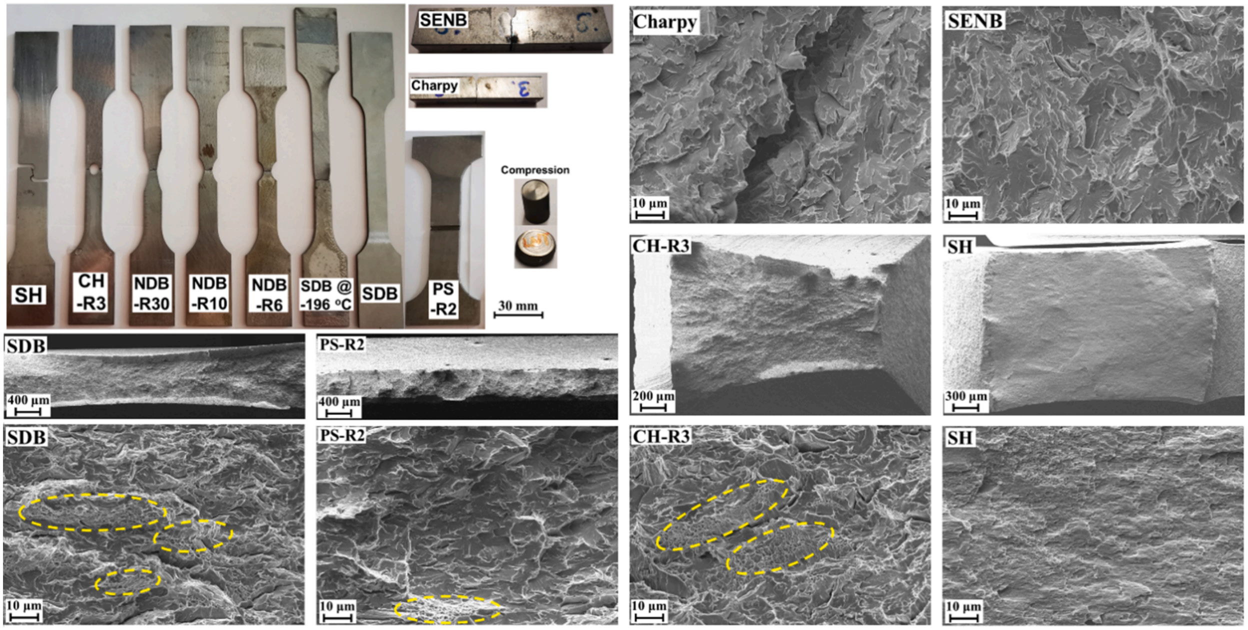

Fig. 4. Overview of fracture surfaces of different specimens tested at –196 °C. The highlighted area indicates the ductile fracture dimples embeded in cleavage facets.

Table 3
Summary of characteristics of experimental fracture properties at –196 °C, and overview of calibration and validation results of numerical simulations.

	Compression	SDB	SH	CH-R3	NDB-R30	NDB-R10	NDB-R6	PS-R2	Charpy	SENB
Enormous plasticity	Yes	Yes	Yes	Yes	Yes	Yes	Yes	Yes	No	No
Failure mechanisms	No fracture	Cleavage dominant	Pure shear	Mixture of ductile and cleavage; cleavage is dominant					Pure cleavage	
Triaxiality	−1/3	1/3~1.0	0.0~0.5	1/3~1.0					1.2~1.5	1.5~1.7
Fracture propagation criterion	–	–	Val. No	Cal. Yes	Val. Yes	Cal. Yes	Val. Yes	Cal. Yes	Val. Yes	Val. Yes
Fracture initiation criterion	–	–	Cal. Yes	Cal. Yes	Val. Yes	Cal. Yes	Val. Yes	Cal. Yes	Val. No	Val. No

slightly larger than the surface. The average length of the fatigue-induced pre-crack ($a/W = 0.5$) was carefully controlled and measured after the fracture in the SENB specimens, as reported by Lian et al. (2015). During the fracture mechanics tests, the crack mouth opening displacements (CMOD) were measured using a clip gage according to ASTM E 1820. Two parallel tests were conducted using the Charpy and SENB specimens with the longitudinal direction along the rolling direction. The through-thickness compression tests were performed at –196 °C using the Rastegaev specimens with a loading velocity of 0.08 mm/min, as shown in Fig. 2, which were filled with lubricant and immersed in liquid nitrogen. The compression tests were terminated after reaching approximately 50% of reduction in the height, and no fracture was observed in the compression tests at –196 °C. These experimental results are direct evidence of the pronounced stress state dependence of fracture behavior at cryogenic temperatures in bcc steels.

2.3. Failure mechanisms across the wide stress states

An overview of the fractured specimens tested at –196 °C is depicted in Fig. 4, which provides direct intuitionistic visualization of the enormous plasticity that occurred in tensile tests at cryogenic temperatures in bcc steels. The fracture surfaces of different specimens have been analyzed using scanning electron microscopy (SEM), as shown in Fig. 4. It is noticed that the failure mechanisms in this bcc steel at –196 °C are changed by the local stress states. Pure shear failure occurs in the SH specimens with a low triaxiality tested at –196 °C, as shown in Fig. 4. In the SENB and Charpy specimens with a very high triaxiality, only cleavage facets are observed on the fracture surfaces, which is a typical brittle fracture in bcc steels tested at –196 °C. In the PS, SDB, NDB, and CH specimens with a moderate local triaxiality, in addition to the dominant cleavage facets, some dimples are also found on the fracture surfaces after testing at –196 °C. As summarized in Table 3, with the increase of local triaxiality from the SH to SENB specimens, the corresponding failure mechanism at –196 °C of this bcc steel is transformed from pure shear failure to pure cleavage fracture. However, in the

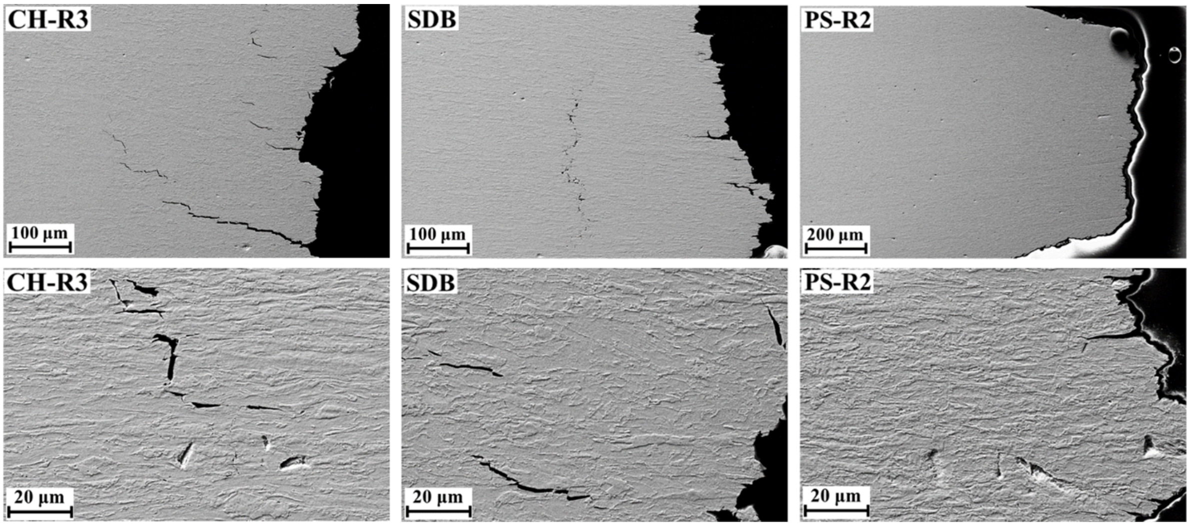

Fig. 5. SEM images of through-thickness cross-section in fractured CH-R3, SDB, and PS-R2 specimens tested at –196 °C.

moderate triaxiality regime, cleavage dominant fracture is triggered only after a significant amount of plastic deformation at –196 °C.

Under loading conditions with a high triaxiality, as in Charpy and SENB specimens, cleavage fracture occurs once the critical value of maximum principal stress σ_1, i.e., the cleavage fracture strength stress σ_c, is reached at the pre-existing defects in the material. Some microcracks are observed in the SEM images taken from the through-thickness planes of three fractured tensile specimens, as shown in Fig. 5. Under tension dominated loading conditions with a moderate triaxiality, the formation of microcracks with a critical length will increase the local triaxiality and σ_1 at the crack tip and lead to cleavage fracture immediately. Therefore, it can be speculated that these critical microcracks are formed right before cleavage fracture after significant plastic deformation in tensile tests of CH-R3, SDB, NDB, and PS specimens. Otherwise, cleavage fracture will be triggered much earlier. In other words, the formation of cracks with a critical length is the critical step of the cleavage fracture in moderate triaxiality regimes at –196 °C, which is a plastic strain controlled process. In the SH geometry, where the critical element experiences shear loading conditions with a low stress triaxiality, critical defects are formed after significant plastic deformation. However, due to the low triaxiality in the SH specimen, the cleavage fracture strength stress σ_c is not reached and the shear failure mechanism leads to final ductile fracture at –196 °C. In compression tests with negative triaxiality, the formation and propagation of cracks are impeded.

3. Constitutive model and fracture criteria

3.1. Evolving plasticity model

To consider the anisotropic effects on the deformation and fracture behavior, the Hill48 (Hill, 1948) yield criterion is applied in the constitutive model. In combination with the non-associated flow rule (Stoughton, 2002), Stoughton and Yoon (2009) have integrated anisotropic hardening into the non-associated Hill48 model, which captures the anisotropic evolution of flow stress. Lian et al. (2018) further extended the evolving non-associated Hill48 (enHill48) model by considering the evolution of Lankford coefficients (r-value) and demonstrated its effectiveness in localization prediction. This study adopted the enHill48 formulation, where the same quadratic equivalent stress $\overline{\sigma}(\boldsymbol{\sigma})$ is used in the yield function f and the flow potential g.

$$f = \overline{\sigma}_{\sigma}(\boldsymbol{\sigma}|F_{\sigma}, G_{\sigma}, H_{\sigma}, L_{\sigma}, M_{\sigma}, N_{\sigma}) - \sigma_{Y}(\overline{\varepsilon}^{p}) \le 0 \tag{1}$$

$$g = \overline{\sigma}_{r}(\boldsymbol{\sigma}|F_{r}, G_{r}, H_{r}, L_{r}, M_{r}, N_{r}) - \sigma_{Y}(\overline{\varepsilon}^{p}) \le 0 \tag{2}$$

$$\overline{\sigma}(\boldsymbol{\sigma}) = \left\{\frac{1}{2}\left[F(\sigma_{22} - \sigma_{33})^2 + G(\sigma_{33} - \sigma_{11})^2 + H(\sigma_{11} - \sigma_{22})^2\right] + L\sigma_{23}^2 + M\sigma_{13}^2 + N\sigma_{12}^2\right\}^{\frac{1}{2}} \tag{3}$$

$$\dot{\boldsymbol{\varepsilon}}^{p} = \dot{\lambda} \cdot \frac{\partial g}{\partial \boldsymbol{\sigma}} \tag{4}$$

$\dot{\lambda}$ is the non-negative plastic multiplier for updating strain components in the non-associated flow rule. The flow stress obtained from uniaxial tensile tests along three loading directions, $\sigma_0(\overline{\varepsilon}^p)$, $\sigma_{45}(\overline{\varepsilon}^p)$, $\sigma_{90}(\overline{\varepsilon}^p)$, is used to calibrate the anisotropic parameters (F_σ, G_σ, H_σ, N_σ) in the yield function. The r-value obtained from uniaxial tensile tests along three loading directions, $r_0(\overline{\varepsilon}^p)$, $r_{45}(\overline{\varepsilon}^p)$, $r_{90}(\overline{\varepsilon}^p)$, is adopted to determine the anisotropic parameters (F_r, G_r, H_r, N_r) in the flow potential. The biaxial flow stress $\sigma_b(\overline{\varepsilon}^p)$ is taken from the through-thickness compression tests, considering the identical deviatoric stress state.

$$
\begin{aligned}
F_\sigma &= \frac{\sigma_0^2(\overline{\varepsilon}^{\mathrm{p}})}{\sigma_{90}^2(\overline{\varepsilon}^{\mathrm{p}})} - 1 + \frac{\sigma_0^2(\overline{\varepsilon}^{\mathrm{p}})}{\sigma_{\mathrm{b}}^2(\overline{\varepsilon}^{\mathrm{p}})} \quad F_{\mathrm{r}} = \frac{2 \cdot r_0(\overline{\varepsilon}^{\mathrm{p}})}{r_{90}(\overline{\varepsilon}^{\mathrm{p}}) \cdot (1 + r_0(\overline{\varepsilon}^{\mathrm{p}}))} \\
G_\sigma &= 1 - \frac{\sigma_0^2(\overline{\varepsilon}^{\mathrm{p}})}{\sigma_{90}^2(\overline{\varepsilon}^{\mathrm{p}})} + \frac{\sigma_0^2(\overline{\varepsilon}^{\mathrm{p}})}{\sigma_{\mathrm{b}}^2(\overline{\varepsilon}^{\mathrm{p}})} \quad G_{\mathrm{r}} = \frac{2}{1 + r_0(\overline{\varepsilon}^{\mathrm{p}})} \\
H_\sigma &= 1 + \frac{\sigma_0^2(\overline{\varepsilon}^{\mathrm{p}})}{\sigma_{90}^2(\overline{\varepsilon}^{\mathrm{p}})} - \frac{\sigma_0^2(\overline{\varepsilon}^{\mathrm{p}})}{\sigma_{\mathrm{b}}^2(\overline{\varepsilon}^{\mathrm{p}})} \quad H_{\mathrm{r}} = \frac{2 \cdot r_0(\overline{\varepsilon}^{\mathrm{p}})}{1 + r_0(\overline{\varepsilon}^{\mathrm{p}})} \\
N_\sigma &= \frac{4 \cdot \sigma_0^2(\overline{\varepsilon}^{\mathrm{p}})}{\sigma_{45}^2(\overline{\varepsilon}^{\mathrm{p}})} - \frac{\sigma_0^2(\overline{\varepsilon}^{\mathrm{p}})}{\sigma_{\mathrm{b}}^2(\overline{\varepsilon}^{\mathrm{p}})} \quad N_{\mathrm{r}} = \frac{2 \cdot (r_0(\overline{\varepsilon}^{\mathrm{p}}) + r_{90}(\overline{\varepsilon}^{\mathrm{p}})) \cdot (r_{45}(\overline{\varepsilon}^{\mathrm{p}}) + 0.5)}{r_{90}(\overline{\varepsilon}^{\mathrm{p}}) \cdot (1 + r_0(\overline{\varepsilon}^{\mathrm{p}}))} \\
L_\sigma &= M_\sigma = 3 \qquad L_{\mathrm{r}} = M_{\mathrm{r}} = 3
\end{aligned}
\tag{5}
$$

3.2. Transformation of σ_1 to critical strain in the space of $(\eta,\ \overline{\theta}, \overline{\varepsilon}^{\mathbf{p}})$

A general stress state can be characterized by stress triaxiality η and Lode angle parameter $\overline{\theta}$, the normalized value of the Lode angle θ ($\overline{\theta} = 1 - \frac{6}{\pi}\theta$) (Bai and Wierzbicki, 2008). These two stress state variables are derived from the three invariants of the Cauchy and deviatoric stress tensor I_1, J_2 and J_3. σ_{m} is the mean stress and $\overline{\sigma}_{\mathrm{v}}$ is the Mises equivalent stress.

$$
\eta = \frac{\sigma_{\mathrm{m}}}{\overline{\sigma}_{\mathrm{v}}} = \frac{I_1}{3\sqrt{3J_2}} \qquad \overline{\theta} = 1 - \frac{2}{\pi}\cos^{-1}\left(\frac{3\sqrt{3}}{2}\frac{J_3}{J_2^{3/2}}\right) \tag{6}
$$

Cleavage fracture occurs only when both the microcrack initiation and crack propagation criteria are met. However, in many cases, the crack propagation is the critical step, and the final cleavage fracture is triggered after reaching the cleavage fracture strength σ_{c}, which is a critical value of the maximum principal stress (Beremin, 1983; Orowan, 1949; Pineau et al., 2016). The maximum principal stress σ_1 can be expressed as a function of stress triaxiality η, Lode angle θ, Lode angle parameter $\overline{\theta}$ and Mises equivalent stress $\overline{\sigma}_{\mathrm{v}}$ (Bai and Wierzbicki, 2010).

$$
\sigma_1 = \sigma_{\mathrm{m}} + s_1 = \sigma_{\mathrm{m}} + \frac{2}{3} \cdot \overline{\sigma}_{\mathrm{v}} \cdot cos\theta = \left(\frac{\sigma_{\mathrm{m}}}{\overline{\sigma}_{\mathrm{v}}} + \frac{2cos\theta}{3}\right) \cdot \overline{\sigma}_{\mathrm{v}} = \left(\eta + \frac{2cos\theta}{3}\right) \cdot \overline{\sigma}_{\mathrm{v}} \tag{7}
$$

$$
\sigma_1 = \left(\eta + \frac{2cos\theta}{3}\right) \cdot \overline{\sigma}_{\mathrm{v}} = \left\{\eta + \frac{2}{3}cos\left[\frac{\pi}{6} \cdot (1 - \overline{\theta})\right]\right\} \cdot \overline{\sigma}_{\mathrm{v}} \tag{8}
$$

For isotropic materials, the Mises equivalent stress $\overline{\sigma}_{\mathrm{v}}$ can be replaced by the corresponding flow stress in the hardening curve.

$$
\overline{\sigma}_{\mathrm{v}} = A \times (\overline{\varepsilon}^{\mathrm{p}} + \varepsilon_0)^n \quad \text{(Swift)} \tag{9}
$$

$$
\overline{\sigma}_{\mathrm{v}} = k_0 + Q \cdot [1 - \exp(-\beta \cdot \overline{\varepsilon}^{\mathrm{p}})] \quad \text{(Voce)} \tag{10}
$$

When $\sigma_1 = \sigma_{\mathrm{c}}$, the maximum principal stress criterion can be converted into the equivalent plastic strain $\overline{\varepsilon}^{\mathrm{p}}$ by substituting the hardening law, which is dependent on the stress triaxiality and Lode angle parameter.

$$
\overline{\varepsilon}^{\mathrm{p}}_{\sigma_1=\sigma_{\mathrm{c}}} = \left(\frac{\sigma_{\mathrm{c}}}{A \cdot \left\{\eta + \frac{2}{3}\cos\left[\frac{\pi}{6} \cdot (1 - \overline{\theta})\right]\right\}}\right)^{\frac{1}{n}} - \varepsilon_0 \quad \text{(Swift)} \tag{11}
$$

$$
\overline{\varepsilon}^{\mathrm{p}}_{\sigma_1=\sigma_{\mathrm{c}}} = -\left\{ln\left[1 - \left(\frac{\sigma_{\mathrm{c}}}{\eta + \frac{2}{3}\cos\left[\frac{\pi}{6} \cdot (1 - \overline{\theta})\right]} - k_0\right) \Big/ Q\right]\right\} \Big/ \beta \quad \text{(Voce)} \tag{12}
$$

For anisotropic materials, the stress state can also be characterized by the invariant based stress triaxiality η and Lode angle parameter $\overline{\theta}$. For the specific case in this study, the reference flow stress is identical to the anisotropic equivalent stress $\overline{\sigma}_\sigma$. The difference between Mises stress $\overline{\sigma}_{\mathrm{v}}$ and Hill48 equivalent stress $\overline{\sigma}_\sigma$ can be determined by the anisotropic stress triaxiality η_{H}, with which the correlation between maximum principal stress σ_1 and equivalent plastic strain $\overline{\varepsilon}^{\mathrm{p}}$ under any specific stress states (characterized by η and $\overline{\theta}$) can be determined.

$$
\eta_{\mathrm{H}} = \frac{\sigma_{\mathrm{m}}}{\overline{\sigma}_\sigma(\boldsymbol{\sigma}|F_\sigma, G_\sigma, H_\sigma, L_\sigma, M_\sigma, N_\sigma)} = \frac{\sigma_{\mathrm{m}}}{\overline{\sigma}_{\mathrm{v}}} \cdot \frac{\overline{\sigma}_{\mathrm{v}}}{\overline{\sigma}_\sigma} = \eta \cdot \frac{\overline{\sigma}_{\mathrm{v}}}{\overline{\sigma}_\sigma} \tag{13}
$$

$$
\sigma_1 = \left\{\eta + \frac{2}{3}\cos\left[\frac{\pi}{6} \cdot (1 - \overline{\theta})\right]\right\} \cdot \frac{\eta_{\mathrm{H}}}{\eta} \cdot [A \times (\overline{\varepsilon}^{\mathrm{p}} + \varepsilon_0)^n] \quad \text{(Swift)} \tag{14}
$$

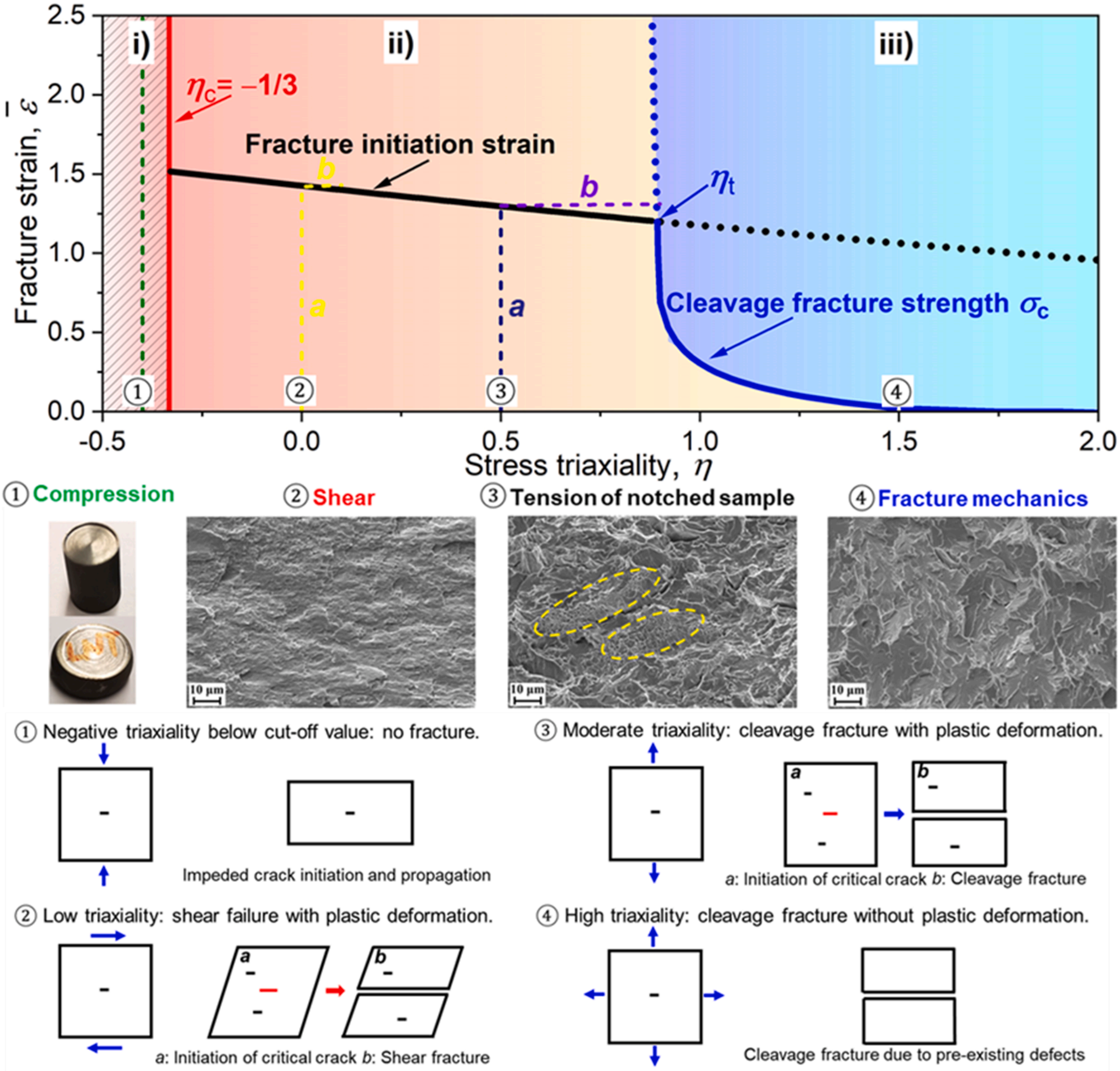

Fig. 6. The schematic illustration of the unified stress state dependent fracture criterion and demonstration of four loading cases.

$$\sigma_1 = \left\{\eta + \frac{2}{3}cos\left[\frac{\pi}{6}\cdot(1-\overline{\theta})\right]\right\}\cdot\frac{\eta_H}{\eta}\cdot\{k_0 + Q\cdot[1-exp(-\beta\cdot\overline{\varepsilon}^p)]\} \quad \text{(Voce)} \tag{15}$$

The derivation of anisotropic triaxiality for Hill48 equivalent stress η_H with respect to principal stress can be found in Park et al. (2017, 2018). As mild anisotropic effects are observed in the strength properties of the investigated material, the Hill48 equivalent stress is approximated by the flow stress during the transformation of σ_1 to criticial equivalent plastic strain in this study.

3.3. A unified stress state dependent fracture criterion

Based on the experimental results, a unified stress state dependent fracture criterion is proposed in this study, which considers the transition of failure mechanisms. The classic local approach to cleavage fracture is established mainly based on the concept of cleavage fracture strength, which provides good predictions for high triaxiality conditions. However, it remains challenging to interpret the cleavage fracture after significant plastic deformation and not applicable for ductile or shear fracture that occurs at the same temperature as cleavage fracture. Considering the weakest link theory of cleavage fracture, the probabilistic distribution of the cleavage fracture strength σ_c is typically expressed using the Weibull distribution function with three parameters, σ_u, $\sigma_{\mathbf{min}}$ and m.

$$\sigma_1 \geq \sigma_c \tag{16}$$

$$P_f = 1 - \exp\left[-\left(\frac{\sigma_c - \sigma_{min}}{\sigma_u - \sigma_{min}}\right)^m\right] \tag{17}$$

The determined cleavage fracture strength locus ($\bar{\varepsilon}^p_{\sigma_1=\sigma_c}$) under a constant Lode angle parameter ($\bar{\theta} = 0$) is demonstrated in Fig. 6 for the investigated material. Given the typical values of cleavage fracture strength and hardening parameters of steels, it is noticed that the required equivalent plastic strain $\bar{\varepsilon}^p_{\sigma_1=\sigma_c}$ to reach the σ_c is extremely high when the local stress triaxiality is low. Accordingly, under some proportional loading conditions in low triaxiality regimes, such as shear ($\eta = 0$) or uniaxial tension ($\eta = \frac{1}{3}$), cleavage fracture will not be triggered by reaching the cleavage fracture strength criterion. However, defects and cracks will be initiated after a certain amount of plastic deformation in typical engineering materials, which leads to the redistribution of stress fields around these defects and the final fracture. As confirmed from the experimental results, critical cracks initiate at the late stage of deformation in tensile tests at –196 °C. Therefore, the cleavage fracture strength criterion with a single parameter σ_c, without considering redistribution of the stress field due to defects initiation, is not sufficient to describe the fracture behavior over a broad range of stress states.

A criterion for the initiation of cracks with a critical length is required. The initiation of critical cracks due to plastic deformation is typically a strain-controlled process, which is affected by the stress states. In uncoupled phenomenological damage mechanics models (Bai and Wierzbicki, 2008, 2010; Ha et al., 2019; Kim et al., 2017; Lou and Yoon, 2017; Mohr and Marcadet, 2015; Mu et al., 2018; Peng et al., 2021; Zhang et al., 2022), fracture initiates when a critical value of plastic strain is reached under proportional loading ($\bar{\varepsilon}^p \geq \bar{\varepsilon}_f$) or the fracture indicator reaches unity for non-proportional loading cases ($I_f = 1$). To compensate for the change of stress state during deformation, average stress triaxiality η_{avg} and average Lode angle parameter $\bar{\theta}_{avg}$ are typically used in the non-proportional loading conditions. As fracture is not observed in the material under uniaxial compression conditions, a cut-off value of the stress triaxiality $\eta_c = -\frac{1}{3}$ is assumed in the strain-based crack initiation criterion (Bao and Wierzbicki, 2005). For more general applications, the Lode angle dependence of cut-off value can be further included (Lou et al., 2014). The phenomenological fracture initiation locus developed for a probabilistic description of fracture (He et al., 2017) is adopted to describe the crack initiation strain $\bar{\varepsilon}_f$ as a function of stress state variables, and it is infinite when the stress triaxiality is below the cut-off value. It is noted that the formulation of the fracture initiation locus in the proposed unified fracture criterion is not exclusive, and alternative ones could be also implemented after proper extension to consider the cleavage fracture and to render the probabilistic nature of fracture, including but not limited to the following ductile fracture initiation models (Bai and Wierzbicki, 2010; Hu et al., 2017; Kim et al., 2017; Li and Fang, 2022; Lou et al., 2014; Mohr and Marcadet, 2015; Mu et al., 2018; Peng et al., 2021). Considering the statistical distribution of plastic strain for the initiation of critical cracks, the Weibull function with three parameters, $\bar{\varepsilon}_{\mathbf{min}}$, $\bar{\varepsilon}_u$ and m, has been adopted to describe the failure probability P_f.

$$\eta_{avg} = \frac{1}{\bar{\varepsilon}^p}\int_0^{\bar{\varepsilon}^p} \eta(\bar{\varepsilon}^p)d\bar{\varepsilon}^p \qquad \bar{\theta}_{avg} = \frac{1}{\bar{\varepsilon}^p}\int_0^{\bar{\varepsilon}^p} \bar{\theta}(\bar{\varepsilon}^p)d\bar{\varepsilon}^p \tag{18}$$

$$\bar{\varepsilon}_f(\eta_{avg}, \bar{\theta}_{avg}) = \begin{cases} +\infty & \eta_{avg} \leq \eta_c \\ \left(F_1 \cdot exp^{-F_2 \cdot \eta_{avg}} - F_3 \cdot exp^{-F_4 \cdot \eta_{avg}}\right) \cdot \bar{\theta}_{avg}{}^2 + F_3 \cdot exp^{-F_4 \cdot \eta_{avg}} & \eta_{avg} > \eta_c \end{cases} \tag{19}$$

$$I_f = \int_0^{\bar{\varepsilon}^p} \frac{d\bar{\varepsilon}^p}{\bar{\varepsilon}_f(\eta_{avg}, \bar{\theta}_{avg})} \tag{20}$$

$$P_f = 1 - \exp\left[-\left(\frac{\bar{\varepsilon}_f - \bar{\varepsilon}_{min}}{\bar{\varepsilon}_u - \bar{\varepsilon}_{min}}\right)^m\right] \tag{21}$$

Significant plastic deformation is only observed in tensile tests with a relatively low triaxiality, and no macroscopic plastic deformation occurs in the Charpy and SENB specimens at –196 °C. Therefore, it is clear that the strain-based fracture initiation criterion (regardless of the different formulations of failure strain in various models) is not valid for the cleavage fracture in high triaxiality regimes at –196 °C. When plotting the fracture initiation strain over triaxiality under a constant Lode angle parameter ($\bar{\theta} = 0$), there is an intersection point with the cleavage fracture strength curve ($\bar{\varepsilon}^p_{\sigma_1=\sigma_c}$), which is defined as a threshold value η_t, as shown in Fig. 6. When local triaxiality is above this threshold value, cleavage fracture is triggered by a limited amount of or even no plastic deformation once the fracture strength σ_c is reached. The strain-controlled initiation of critical cracks is a more critical step when local triaxiality is below this threshold value. When demonstrated in the space of equivalent plastic strain, triaxiality, and Lode angle parameter, the threshold boundary is defined as the intersection of the fracture initiation locus (η, $\bar{\theta}$, $\bar{\varepsilon}_f$) with the surface of cleavage fracture strength (η, $\bar{\theta}$, $\bar{\varepsilon}^p_{\sigma_1=\sigma_c}$). The threshold triaxiality η_t under a given Lode angle parameter $\bar{\theta}$ can be determined according to Eqs. (22) and (23). The threshold value of stress triaxiality η_t is a material parameter that is dependent on the hardening capacity and the crack propagation resistance property σ_c of the material, which is affected by temperature, strain rate, and microstructure.

Table 4
Calibrated plasticity parameters at room temperature and –196 °C (Lankford coefficients taken from Shen et al. (2020b), and units of parameters a, b, A, k_0, Q: MPa).

RT				–196 °C				RT and –196 °C			
	σ_0	σ_{45}	σ_{90}		σ_0	σ_{45}	σ_{90}		r_0	r_{45}	r_{90}
$\sigma = a\cdot\bar{\varepsilon}^{p} + b$ $(0 \le \bar{\varepsilon}^{p} < 0.02)$				$\sigma = a\cdot\bar{\varepsilon}^{p} + b$ $(0 \le \bar{\varepsilon}^{p} < 0.05)$				$r = R\cdot\exp(S\cdot\bar{\varepsilon}^{p})$			
a	1650.0	1026.0	1838.0	a	402.1	217.7	481.8	R	0.593	1.068	0.783
b	536.6	534.1	561.2	b	938.3	905.0	978.9	S	0.263	0.824	–0.786
$\sigma = A\times(\bar{\varepsilon}^{p} + \varepsilon_0)^{n}$ $(0.02 \le \bar{\varepsilon}^{p})$				$\sigma = k_0 + Q\cdot(1-\exp(-\beta\cdot\bar{\varepsilon}^{p}))$ $(0.05 \le \bar{\varepsilon}^{p})$							
A	931.8	907.2	946.5	k_0	870.1	828.0	921.5				
ε_0	0.002	0.000	0.004	Q	520.6	519.7	478.2				
n	0.130	0.125	0.124	β	4.687	4.560	4.916				

$$\bar{\varepsilon}_{\mathrm{f}}(\eta_{\mathrm{t}}, \bar{\theta}) = \bar{\varepsilon}^{\mathrm{p}}_{\sigma_1=\sigma_{\mathrm{c}}} = \left(\frac{\sigma_{\mathrm{c}}}{A\cdot\left\{\eta_{\mathrm{t}} + \frac{2}{3}\cos\left[\frac{\pi}{6}\cdot(1-\bar{\theta})\right]\right\}}\right)^{\frac{1}{n}} - \varepsilon_0 \quad \text{(Swift)} \tag{22}$$

$$\bar{\varepsilon}_{\mathrm{f}}(\eta_{\mathrm{t}}, \bar{\theta}) = \bar{\varepsilon}^{\mathrm{p}}_{\sigma_1=\sigma_{\mathrm{c}}} = -\left\{ln\left[1-\left(\frac{\sigma_{\mathrm{c}}}{\eta_{\mathrm{t}} + \frac{2}{3}\cos\left[\frac{\pi}{6}\cdot(1-\bar{\theta})\right]} - k_0\right)\Big/ Q\right]\right\}\Big/\beta \quad \text{(Voce)} \tag{23}$$

By introducing a binary variable D, i.e., zero for undamaged and one for damage conditions, the damage status of the material can be described by the unified fracture criterion.

$$D = \begin{cases} 0 & \eta \le \eta_{\mathrm{c}} \quad \text{i)No fracture} \\ \left.\begin{matrix} 0 & I_{\mathrm{f}} < 1 \wedge \eta_{\mathrm{c}} < \eta < \eta_{\mathrm{t}} \\ 1 & I_{\mathrm{f}} \ge 1 \wedge \eta_{\mathrm{c}} < \eta < \eta_{\mathrm{t}} \end{matrix}\right\} & \text{ii)Critical step : fracture initiation} \\ \left.\begin{matrix} 0 & \sigma_1 < \sigma_{\mathrm{c}} \wedge \eta_{\mathrm{t}} \le \eta \\ 1 & \sigma_1 \ge \sigma_{\mathrm{c}} \wedge \eta_{\mathrm{t}} \le \eta \end{matrix}\right\} & \text{iii)Critical step : fracture propagation} \end{cases} \tag{24}$$

The unified fracture criterion is demonstrated as fracture strain over stress triaxiality for a constant Lode angle parameter in Fig. 6, where the fracture properties under four representative loading conditions are elaborated. Depending on the failure mechanisms, the stress state space can be divided into three regimes with different ranges of stress triaxiality according to this fracture criterion. For the loading conditions with a negative triaxiality below the cut-off value ($\eta \le \eta_c$) in the (i) regime, no fracture occurs as both fracture initiation and propagation are impeded. For loading conditions above the threshold triaxiality value ($\eta_t \le \eta$) in the (iii) regime, the cleavage fracture strength can be reached at pre-existing defects with a small amount of local plasticity due to the very high triaxiality. Due to the stochastic distribution of pre-existing defects in the material, a pronounced scatter is usually observed in the cleavage fracture properties determined from high triaxiality experiments. Therefore, the stress-driven cleavage fracture propagation crossing different barriers is the critical step of cleavage fracture in a high triaxiality regime. For loading conditions within the ii) regime with low to moderate triaxiality ($\eta_c < \eta < \eta_t$), fracture occurs after significant plastic deformation as the initiation of cracks with a critical length is the critical step. Nevertheless, the underlying failure mechanisms might change with local stress states in the (ii) regime. Under loading conditions with moderate triaxiality, cleavage fracture strength is not reached at pre-existing defects in the initial loading stage, which is demonstrated as stage *a* in Fig. 6. With increasing plastic deformation, initiation of cracks with a critical length occurs, and local stress triaxiality at the crack tip increases, which is interpreted as stage *b*. Therefore, cleavage fracture strength can be reached immediately at these critical cracks, leading to cleavage fracture with significant plastic deformation. In low triaxiality scenarios, such as shear, the cleavage fracture strength is still not reached after the initiation of critical cracks, and the final fracture occurs due to the shear failure mechanism. In other words, after critical cracks are initiated due to plastic deformation, which failure mechanism, i.e., shear or cleavage fracture, will be triggered is determined by the local values of stress states and σ_1. Since the initiation of critical cracks is a strain-controlled process, no pronounced scatter is observed in fracture properties under loading conditions within a low to moderate triaxiality regime. The observed fracture behavior with or without plastic deformation at –196 °C can be explained with the developed unified fracture criterion. In addition, the transition of failure mechanisms at the same temperature with stress states can also be explained with this theory, which can be applied to other similar materials.

4. Parameters calibration in the anisotropic plasticity model

Anisotropic plasticity parameters are determined for both RT and –196 °C by calibrating the individual flow curves and r-value evolution functions along three directions. To obtain a high fidelity, the hardening behavior within the Lüders strain range is approximated by a linear function, which is followed by a Swift hardening law for RT and a Voce hardening law for –196 °C. In

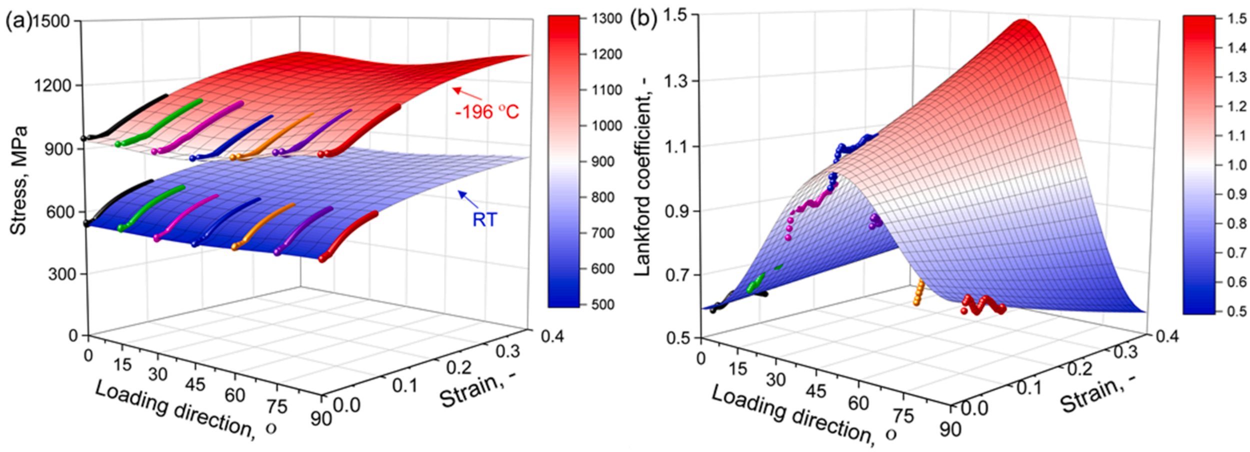

Fig. 7. Experimental (curves) and predicted (surfaces) anisotropic distribution of (a) flow stress and (b) Lankford coefficients at room temperature and –196 °C (experimental results available in Shen et al. 2020b).

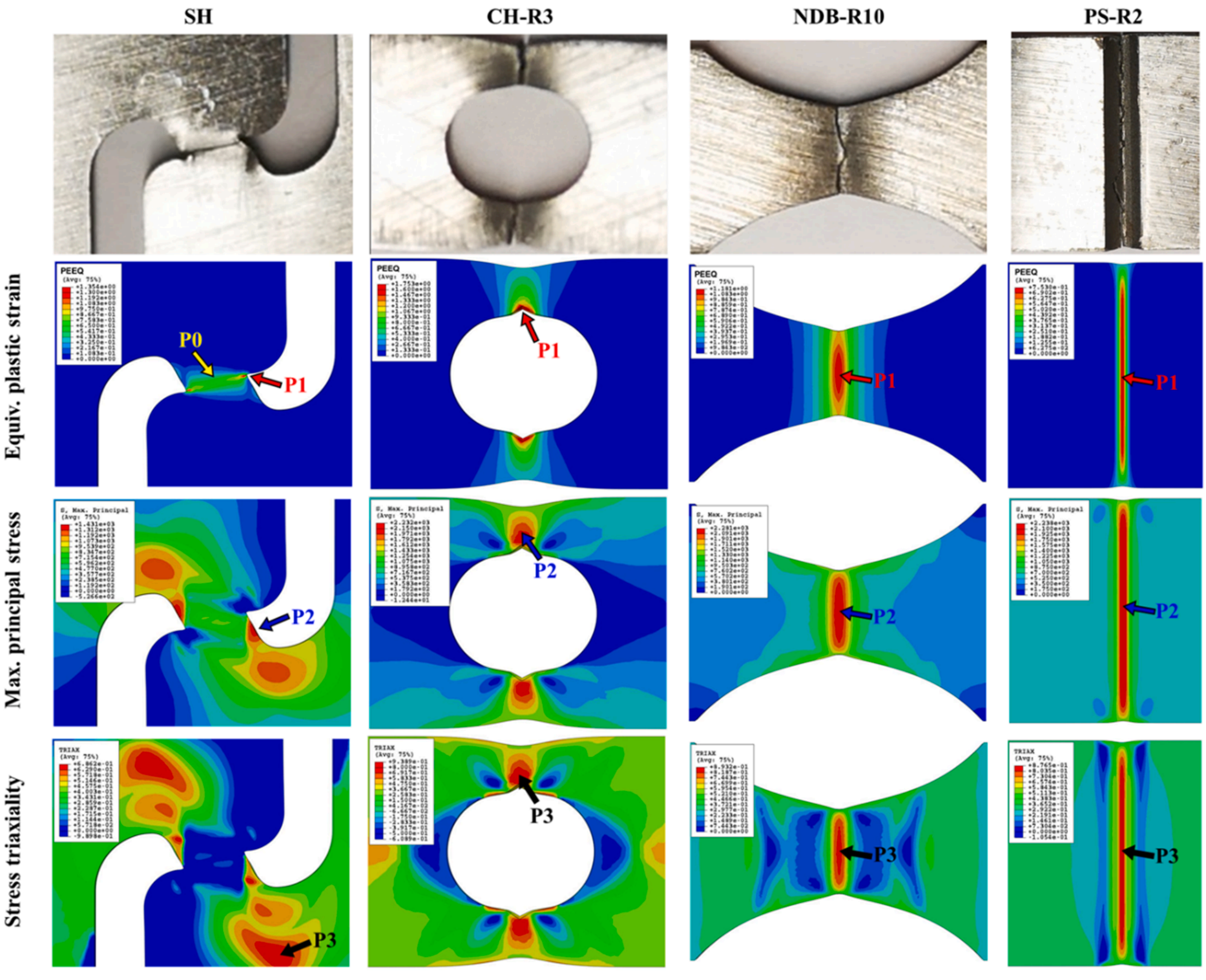

Fig. 8. Distribution of strain and stress variables on the mid-thickness plane in four tensile samples at fracture moment at –196 °C.

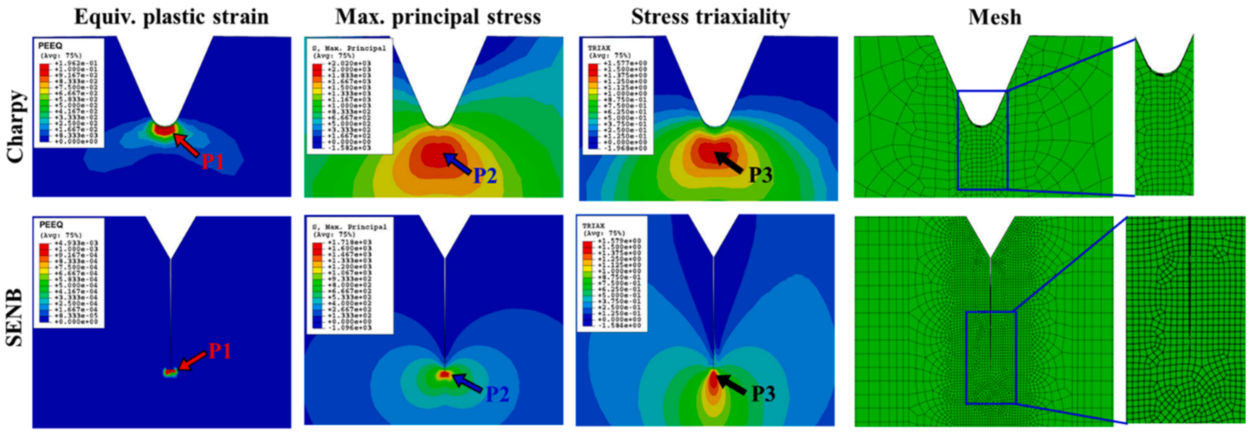

Fig. 9. Distribution of strain and stress variables on the mid-thickness plane in the Charpy and SENB samples at fracture point at –196 °C.

Table 5
Summary of local stress and strain variables at fracture from critical elements of tensile specimens in fracture initiation criterion at –196 °C.

Specimen	η_{avg}	$\overline{\theta}_{avg}$	$\overline{\varepsilon}_f^p$ (P_f=5%)	σ_1 (MPa) (P_f=5%)	$\overline{\varepsilon}_f^p$ (P_f=50%)	σ_1 (MPa) (P_f=50%)	$\overline{\varepsilon}_f^p$ (P_f=95%)	σ_1 (MPa) (P_f=95%)
CH-R3 (P1)	0.471	0.722	1.872	1651	1.946	1689	2.013	1724
NDB-R30 (P1)	0.599	0.634	1.039	2109	1.153	2230	1.253	2343
NDB-R10 (P1)	0.625	0.581	1.076	2221	1.157	2277	1.233	2329
NDB-R6 (P1)	0.661	0.524	0.977	2169	1.245	2268	1.489	2363
PS-R2 (P1)	0.775	0.295	0.645	2153	0.761	2237	0.867	2315
SH (P0)	−0.003	0.021	0.692	798	0.756	830	0.814	862

addition, the biaxial flow curve is calibrated from through-thickness compression tests, which is $\sigma_b = 880.5 \times (\overline{\varepsilon}^p + 0.001)^{0.105}$ for RT and $\sigma_b = 1041.1 + 803.9 \cdot (1 - \exp(-2.511 \cdot \overline{\varepsilon}^p))$ for –196 °C, respectively. The calibrated hardening parameters are summarized in Table 4. The experimental results along seven loading directions are shown as dotted curves in Fig. 7. As the anisotropic parameters (F_σ, G_σ, H_σ, N_σ) evolve with the plastic strain $\overline{\varepsilon}^p$ according to Eq. (5), the flow stress along other loading directions can be explicitly predicted with the applied evolving plasticity model, as depicted by the surface in Fig. 7(a). It is observed from experimental results that the anisotropic distribution pattern of strength is not significantly affected by temperature in this material (Shen et al., 2020a), as shown in Fig. 1, indicating the shape of the yield locus is not affected by temperature. Since the Lankford coefficients are mainly controlled by the shape (slope) of the flow potential, it is reasonable to assume the Lankford coefficients are independent of temperature as well. To determine the evolution of the flow potential, an exponential function is adopted to fit the measured Lankford coefficients, $r_0(\overline{\varepsilon}^p)$, $r_{45}(\overline{\varepsilon}^p)$, $r_{90}(\overline{\varepsilon}^p)$, in uniaxial tensile tests along three loading directions at RT (Shen et al., 2020b). With calibrated anisotropic parameters (F_r, G_r, H_r, N_r) in the flow potential, the evolution of Lankford coefficients with plastic strain along other directions can be accurately predicted, as depicted by the surface in Fig. 7(b). Validation of the calibrated plasticity parameters is based on the accurate prediction of force and displacement curves in different tensile tests.

5. Fracture prediction

The constitutive model and fracture criteria are implemented as a VUMAT user subroutine. Crack formation and propagation are achieved by the element deletion method in the finite element simulations using the ABAQUS/Explicit software. To calibrate the fracture model for the investigated material, the critical local stress and strain variables need to be collected for different loading conditions. Finite element simulations of tensile deformation using different sample geometries, three-point bending tests using Charpy specimens and SENB specimens at –196 °C have been performed using the calibrated evolving plasticity model. In the finite element model of the SENB specimen, a pre-crack with half-length of the thickness ($a/W = 0.5$) is assigned. A fine mesh ($0.1 \times 0.1 \times 0.1$ mm^3) has been assigned in the critical region, and half-thickness symmetry has been applied in all specimens with solid elements (C3D8R). The distribution of local stress and strain variables on the mid-thickness plane at fracture displacements is depicted in Fig. 8 for four tensile geometries (SH, CH-R3, NDB-R10, and PS-R2), and in Fig. 9 for Charpy and SENB specimens. The maximum value of equivalent plastic strain, maximum principal stress σ_1 and stress triaxiality is located at the position P1, P2, and P3, respectively. The local stress and strain variables from these defined critical elements are used to calibrate the unified fracture model. As strain-controlled crack initiation is the critical step in low to moderate triaxiality regimes, the four tensile geometries (SH, CH-R3, NDB-R10, and PS-R2) are used to calibrate the fracture initiation criterion. According to the crack propagation path shown in Fig. 8, the critical element for crack initiation is taken from position P0 (with a local shear stress state) in the SH specimen and P1 in other geometries. For the stress-driven crack propagation criterion, the critical elements at position P2 in the CH, NDB, and PS geometries are

Table 6
The parameters in the Weibull distribution function of fracture strain from critical elements of tensile specimens in fracture initiation criterion at –196 °C.

Specimen	CH-R3 (P1)	NDB-R30 (P1)	NDB-R10 (P1)	NDB-R6 (P1)	PS-R2 (P1)	SH (P0)
$\bar{\varepsilon}_{\mathbf{min}}$	1.796	0.917	0.987	0.689	0.520	0.624
$\bar{\varepsilon}_{u}$	1.960	1.173	1.173	1.297	0.783	0.769
m	4.0	4.0	4.0	4.0	4.0	4.0

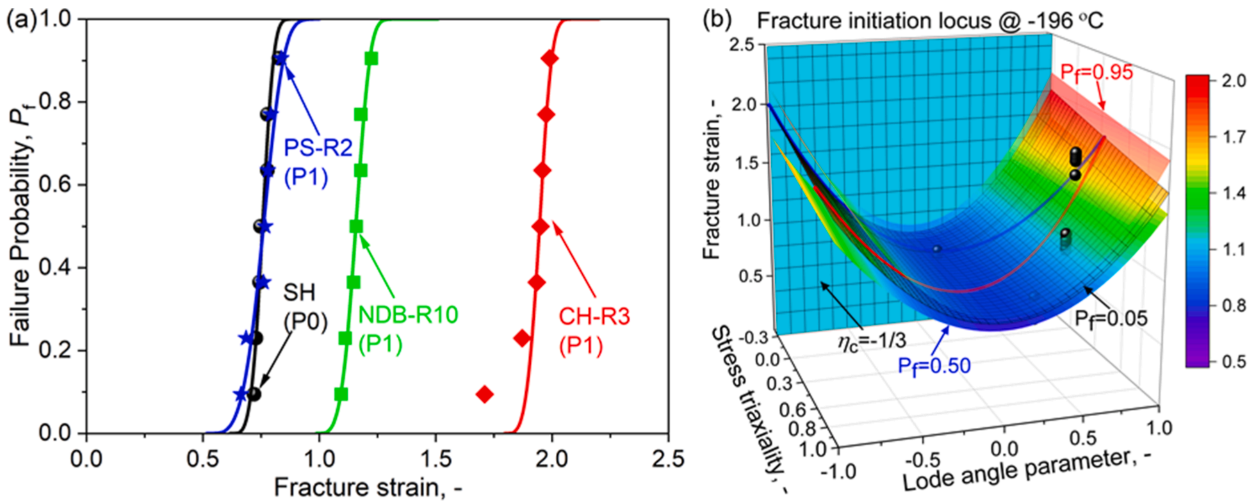

Fig. 10. The probabilistic distribution of fracture initiation strain in different tensile geometries (a) and the fracture initiation locus corresponding to three failure probabilities (b) at –196 °C.

Table 7
The calibrated parameters in the unified fracture criterion corresponding to three failure probabilities at –196 °C.

Specimen	F_1	F_2	F_3	F_4	σ_c (MPa)
P_f=5%	1.70	0.12	0.76	0.01	2155
P_f=50%	1.93	0.14	0.82	0.02	2255
P_f=95%	2.10	0.09	0.88	0.04	2340

used to estimate the cleavage fracture strength. The model calibration and validation strategy and evaluation of numerical results are summarized in Table 3.

5.1. Strain based fracture initiation criteria

Despite the phenomenon that failure mechanisms can be different (pure shear failure or cleavage dominant fracture) after significant plastic deformation in low to moderate triaxiality regimes, a common feature is that the strain-controlled initiation of cracks with a critical length is the critical step under these loading conditions. For the reason of completeness, the average stress triaxiality η_{avg}, average Lode angle parameter $\bar{\theta}_{\text{avg}}$, fracture strain $\bar{\varepsilon}_f^p$ and maximum principal stress σ_1 at fracture moment extracted from the critical elements in these tensile specimens are summarized in Table 5. The accumulative failure probability concept has been adopted to determine fracture strain by using the three-parameter Weibull distribution function. As seven parallel tests have been performed for all tensile geometries at –196 °C, the accumulative failure probability for each test is calculated as $P_f^j = \frac{j-0.3}{N+0.4}$. N is the total number of parallel tests, and j is the sequence number sorted according to the fracture displacement. The calibrated Weibull distribution parameters of fracture strain for each geometry are summarized in Table 6.

The distribution of fracture strain in four tensile geometries (SH, CH-R3, NDB-R10, and PS-R2) at –196 °C is depicted in Fig. 10. Given the calibrated Weibull distribution parameters for each geometry, the fracture initiation strain at three specific failure probabilities (P_f = 5%, 50% and 95%) can be determined and summarized in Table 5. The local stress and strain variables from four tensile geometries (SH, CH-R3, NDB-R10, and PS-R2) are used to determine the fracture initiation locus at –196 °C corresponding to three failure probabilities, as shown in Fig. 10. The determined parameters in the strain-based fracture initiation criteria corresponding to three different failure probabilities are summarized in Table 7. Considering the fact that no fracture is observed in the compression tests at –196 °C, the cut-off value of $\eta_c = -\frac{1}{3}$ is adopted in the strain criterion. As shown in Fig. 11, the fracture displacements in all

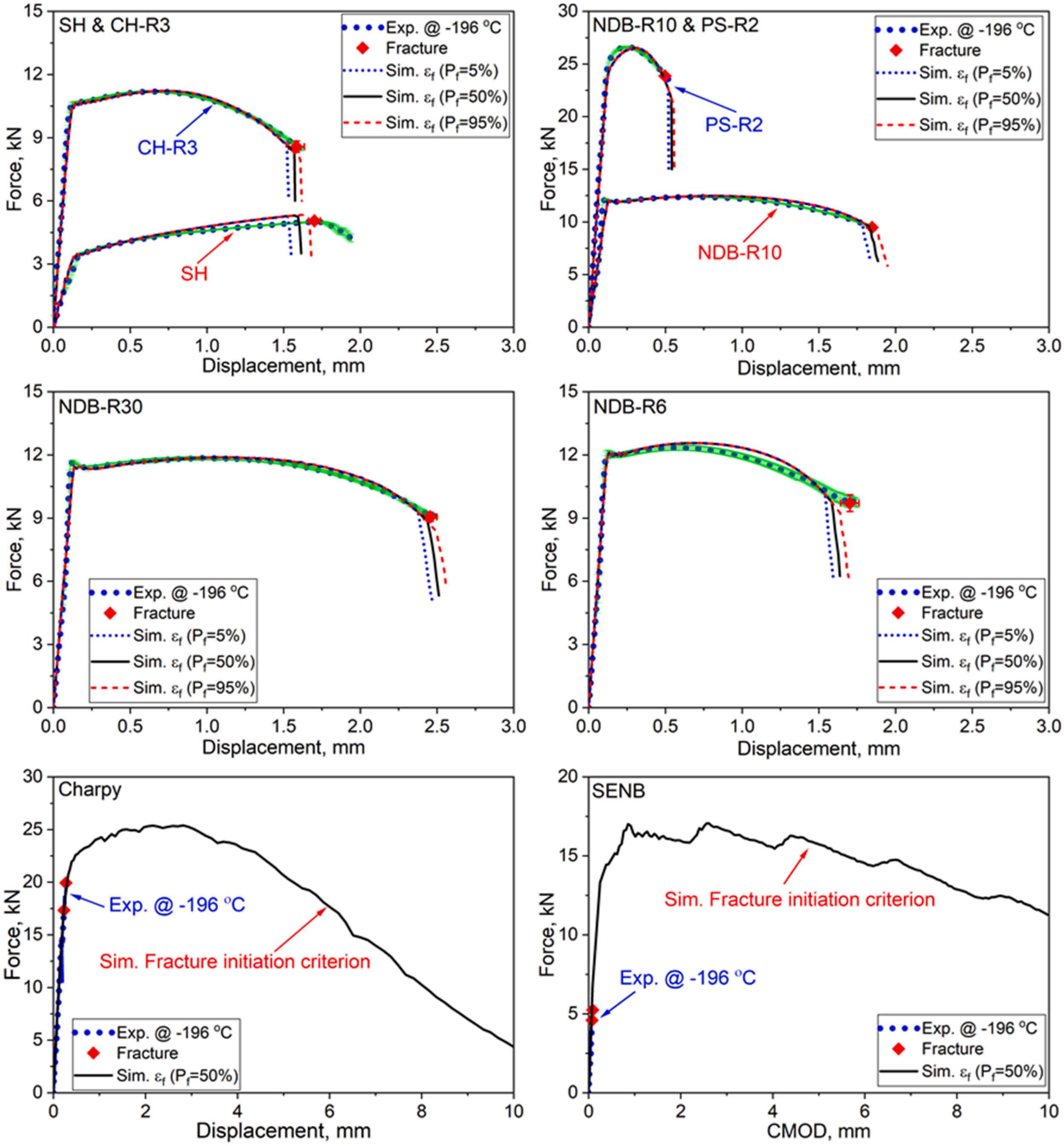

Fig. 11. Prediction of global force–displacement results in tensile tests, three-point bending tests using Charpy specimens, and SENB fracture mechanics tests at –196 °C using strain-based fracture initiation criteria.

tensile tests at –196 °C can be well captured by the fracture initiation criterion. However, when the fracture initiation criterion corresponding to a failure probability of 50% is applied in the three-point bending tests using Charpy and SENB specimens, a significant overestimation of fracture displacements is observed in the simulation results.

Despite the global force and displacement response in all tensile specimens can be predicted by the fracture initiation criterion, it has to be emphasized that the underlying failure mechanism is different, which is a shear failure in the SH geometry and cleavage dominant fracture in other tensile specimens. Strain-based fracture initiation criterion is widely used to describe shear failure in typical damage mechanics approaches. The calibrated fracture initiation criterion is used to describe the phenomenon that cleavage fracture occurs immediately after the initiation of critical cracks during tensile deformation of other specimen geometries at –196 °C. In other words, cleavage fracture could occur at early displacements in tensile tests of CH, NDB, and PS geometries if critical cracks have

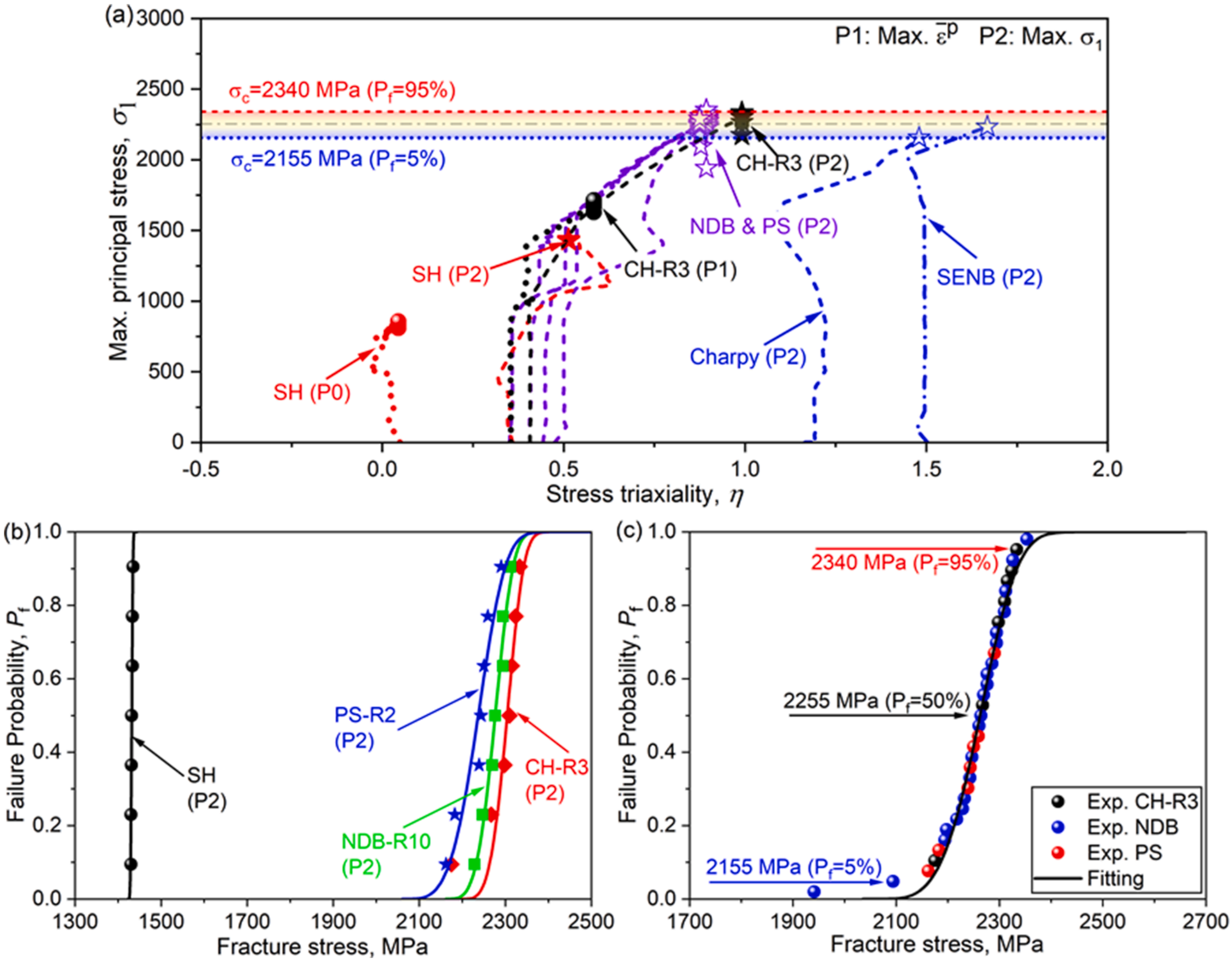

Fig. 12. Evolution of the maximum principal stress σ_1 at critical positions (a), and Weibull distribution of fracture stress in (b) individual geometries and (c) combined results of CH, NDB, and PS geometries tested at –196 °C.

Table 8
Summary of local stress and strain variables from critical elements with the maximum value of σ_1 at fracture moment in tensile specimens at –196 °C.

Specimen	η	$\bar{\theta}$	$\bar{\varepsilon}^p$ (P_f=5%)	σ_1 (MPa) (P_f=5%)	$\bar{\varepsilon}^p$ (P_f=50%)	σ_1 (MPa) (P_f=50%)	$\bar{\varepsilon}^p$ (P_f=95%)	σ_1 (MPa) (P_f=95%)
CH-R3 (P2)	0.992	0.996	1.073	2253	1.168	2305	1.259	2353
NDB-R30 (P2)	0.878	0.599	1.039	2109	1.153	2230	1.253	2343
NDB-R10 (P2)	0.897	0.511	1.076	2221	1.157	2277	1.233	2329
NDB-R6 (P2)	0.893	0.577	0.977	2169	1.245	2268	1.489	2363
PS-R2 (P2)	0.875	0.427	0.645	2153	0.761	2237	0.867	2315
SH (P2)	0.513	0.380	0.352	1428	0.363	1431	0.372	1435

initiated at smaller strain values. Due to the high local triaxiality in both Charpy (η = 1.48) and SENB (η = 1.67) specimens, crack initiation is not the critical step. Therefore, the calibrated fracture initiation locus should not be extrapolated to high triaxiality regimes, where no macroscopic plastic deformation occurs at –196 °C.

5.2. Cleavage fracture strength criteria

The final cleavage fracture is triggered in bcc structures at cryogenic temperatures when the cleavage fracture strength σ_c is reached, which is the critical value of the maximum principal stress σ_1. The maximum value of σ_1 at the fracture displacement is located at position P2 in all specimens, as shown in Figs. 8 and 9. It is noticed that the location of the maximum σ_1 (P2) is identical to the location of the maximum equivalent plastic strain (P1) in NDB and PS geometries, which is at the symmetry center. For the CH-R3

Table 9
The parameters in the Weibull distribution function of fracture stress from critical elements of tensile specimens in stress criterion at –196 °C.

Specimen	CH-R3 (P2)	NDB-R30 (P2)	NDB-R10 (P2)	NDB-R6 (P2)	PS-R2 (P2)	SH (P2)	CH, PS, NDB (P2)
$\sigma_{\mathbf{min}}$ (MPa)	2197	1975	2161	2060	2061	1424	2053
σ_u (MPa)	2315	2253	2288	2289	2254	1433	2274
m	4.0	4.0	4.0	4.0	4.0	4.0	4.0

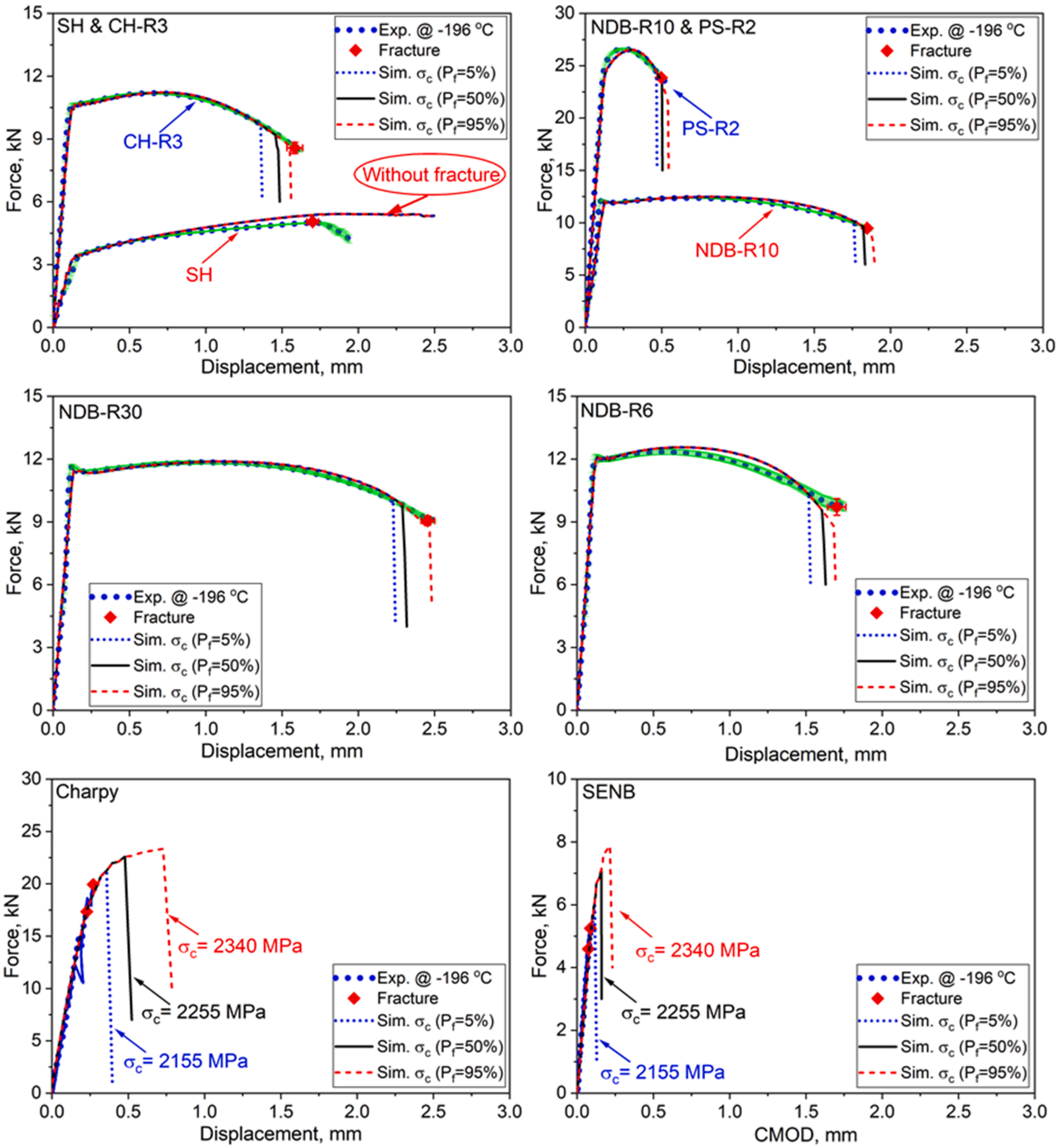

Fig. 13. Prediction of force–displacement results in tensile tests, three-point bending tests using Charpy specimens, and SENB fracture mechanics tests at –196 °C using the cleavage fracture strength criteria.

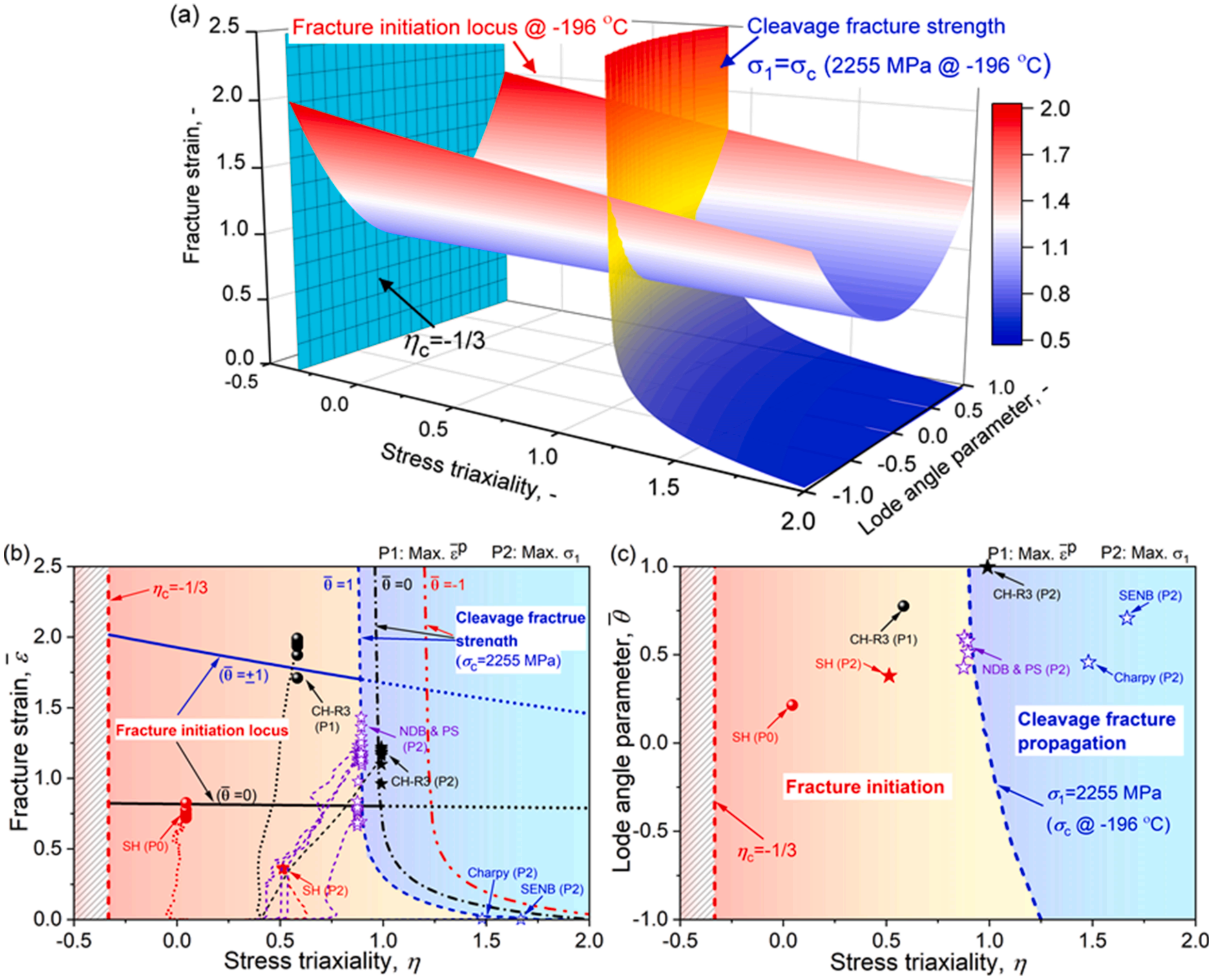

Fig. 14. The calibrated unified fracture criterion at −196 °C. (a) Demonstrated in the three-dimensional space of fracture strain, triaxiality, and Lode angle parameter; Projection in the two-dimensional space: (b) fracture strain vs. stress triaxiality and (c) Lode angle parameter vs. stress triaxiality.

specimen, the position of the maximum equivalent plastic strain (P1) is located at the notch root, while the position corresponding to the maximum σ_1 (P2) is slightly shifted from the notch root due to necking effects. The evolution of σ_1 with stress triaxiality at the critical positions of different specimens is shown in Fig. 12(a). Since crack propagation takes place instantaneously once the cleavage fracture strength σ_c is reached, the instantaneous values of local stress and strain variables (η, $\overline{\theta}$, $\overline{\varepsilon}^p$, σ_1) at the fracture moment are extracted from critical elements at position P2, as summarized in Table 8. Three-parameter Weibull function is applied to describe the probabilistic distribution of fracture stress for each geometry, and calibrated parameters are summarized in Table 9. As shown in Fig. 12, the maximum value of σ_1 at fracture in the SH specimen is significantly lower than other geometries, which is consistent with the observed different failure mechanisms at −196 °C. Since cleavage fracture is not triggered in the SH specimen, the values of σ_1 at fracture moment in other tensile specimens including CH-R3, NDB, and PS geometries are combined and sorted ascendingly to determine the cleavage fracture strength σ_c of the investigated material, as shown in Fig. 12. The cleavage fracture strength σ_c at three failure probabilities is summarized in Table 7. From the evolution of σ_1 demonstrated in Fig. 12(a), it is also noticed that the cleavage fracture strength is reached in both Charpy and SENB specimens with a high triaxiality, where only negligible plastic deformation occurs.

When the cleavage fracture strength criterion with a single parameter σ_c is applied, the fracture properties under high triaxial loading conditions can be predicted, as shown in Fig. 13. The deviation in the predicted fracture behavior in the Charpy and SENB specimens under three-point bending configurations is mainly attributed to limited fidelity in the description of stress and strain fields ahead of the sharp crack and notch using the current mesh strategy ($0.1 \times 0.1 \times 0.1$ mm^3 in the critical region). The predicted fracture displacements in tensile tests are in line with experimental results except for the SH geometry due to the different failure mechanisms. It is important to notice the determined fracture strength, based on macroscopic finite element simulations in this study, is only an estimation of the *technical* cleavage fracture strength value, as the redistribution of stress fields at crack tips is not taken into consideration. Therefore, a larger deviation is observed in the predicted fracture displacements when the crack initiation is more critical, such as in the CH-R3 and NDB-R30 geometries. Since the maximum principal stress σ_1 has reached a sufficiently high value at the critical positions in CH, NDB, and PS specimens, cleavage fracture is triggered immediately once the initiation criterion of critical cracks is met during plastic deformation. However, cleavage fracture is not triggered even after the initiation of critical cracks in the SH specimen due to low σ_1 value, which is consistent with the simulation results that no fracture is predicted in the SH specimen when cleavage fracture strength σ_c is used as the only failure criterion. These numerical results are consistent with the observed different failure mechanisms in tensile tests at –196 °C. In summary, the cleavage fracture strength criterion with a single parameter σ_c is not applicable to describe the failure properties under loading conditions with low stress triaxialities.

5.3. The unified fracture model

The unified fracture model is established by integrating the fracture initiation criterion and the cleavage fracture strength criterion, which considers the transition of failure mechanism in bcc steels at –196 °C over a broad spectrum of stress states. For the reason of simplicity, the concept of this unified fracture model corresponding to a specific failure probability ($P_f = 50\%$) is elaborated, as shown in Fig. 14. It is observed that decreasing plastic strain is required to trigger fracture with the increase of local stress triaxiality. Due to the transition of failure mechanisms, a sharp change of failure strain occurs at the threshold stress states.

For demonstration purposes, the transformation of cleavage fracture strength to equivalent plastic strain ($\overline{\varepsilon}^{p}_{\sigma_1=\sigma_c}$), which is dependent on stress triaxiality and Lode angle parameter, has been derived from the hardening law of the material at –196 °C, neglecting the mild anisotropic effects. However, it needs to be pointed out that the cleavage fracture propagation criterion is implemented as a critical value of the maximum principal stress in the numerical simulations, which is not affected by the transformation strategy. The surface corresponding to cleavage fracture strength ($\sigma_c = 2255$ MPa @ $P_f = 50\%$) shows a very sharp transition with the increase of triaxiality, as demonstrated in Fig. 14(a). In high stress triaxiality regime, the cleavage fracture strength σ_c can be reached with little plastic strain, leading to macroscopic brittle fracture. With decreasing triaxiality, the cleavage fracture strength criterion is more difficult to reach as the corresponding equivalent plastic strain increases rapidly and approaches the infinite. The intersection of the fracture initiation strain locus ($P_f = 50\%$) and the surface of cleavage fracture strength (σ_c @ $P_f = 50\%$) is determined as the threshold boundary in the proposed unified fracture criterion at –196 °C. When the local stress triaxiality is below the threshold value η_t, the initiation of critical cracks occurs after plastic deformation according to the strain-based fracture initiation criterion. Depending on the value of local stress triaxiality and σ_1, either cleavage fracture or shear failure will be triggered after the initiation of critical cracks. When the local stress triaxiality is below the cut-off value of $\eta_c = -\frac{1}{3}$, neither crack initiation nor crack propagation occurs, which explains the phenomenon that no fracture is observed even after significant plastic deformation in uniaxial compression tests at –196 °C.

The projection of this unified fracture criterion at –196 °C is demonstrated in Fig. 14. The fracture initiation locus and fracture strength locus ($\sigma_c = 2255$ MPa) corresponding to the failure probability of $P_f = 50\%$ are demonstrated for constant Lode angle parameters ($\overline{\theta} = 0, \pm 1$) in Fig. 14(b). The deformation history of critical elements corresponding to the maximum equivalent plastic strain (P1) and the maximum σ_1 (P2) is demonstrated for different specimens. Due to the high local stress triaxiality, the cleavage fracture strength is reached immediately with negligible local plastic deformation in Charpy and SENB specimens. Due to the strain hardening and evolution of stress states during deformation (i.e., increase of stress triaxiality), the critical value of σ_1 is eventually reached in the critical elements of CH, NDB, and PS geometries after a significant amount of plastic deformation at –196 °C. However, the maximum value of σ_1 is still significantly below cleavage fracture strength σ_c in the SH geometry. Therefore, cleavage fracture is triggered in the CH, NDB, and PS specimens after critical cracks are initiated, and shear failure occurs in the SH specimen at –196 °C.

The top-view projection of the unified fracture criterion is shown in Fig. 14(c), where the instantaneous stress triaxiality and Lode angle parameter of critical elements in different geometries at fracture moment are depicted as well. As shown in Fig. 14(c), the stress state space can be divided into three regimes depending on the underlying failure mechanisms: (i) fracture does not occur when triaxiality is below the cut-off value of $\eta_c = -\frac{1}{3}$; (ii) initiation of critical cracks is the critical step of fracture in the low to moderate range of triaxiality; (iii) stress-driven crack propagation crossing various barriers is the critical step of cleavage fracture in a high triaxiality regime. The boundary between regimes (ii) and (iii) is determined by the hardening capacity and crack resistance of the material, which is affected by temperature, strain rate, microstructure, etc. In this regard, it is theoretically feasible to trigger pure ductile fracture mechanisms (100% dimples on fracture surface due to void nucleation, growth, and coalescence) in the bcc steel at –196 °C by maintaining a tension-dominated loading path with the triaxiality below the threshold value η_t. However, once a crack is formed due to plastic deformation, a sudden increase in local triaxiality and σ_1 near the crack tip might eventually lead to the cleavage fracture, which results in the coexistence of dimples and cleavage facets on the fracture surfaces of tensile specimens. When the stress triaxiality is further decreased into the shear-dominated failure regime, cleavage crack propagation is completely inhibited, and the shear failure mechanism is finally activated. Typical ductile to brittle transition properties in bcc structures are mainly determined by Charpy and fracture mechanics tests with high local triaxiality values to obtain conservative results. This study provides the first experimental evidence and explanations of the impacts of stress states on the transition of failure mechanisms in bcc materials. The reported fracture phenomena with or without enormous ductility at –196 °C are not exclusive features of this X70 steel, which should be a general fracture pattern in similar materials that can be explained by the proposed unified fracture criterion.

The proposed fracture criterion is calibrated and validated based on experimental results obtained at –196 °C in this study. However, this fracture criterion can also be applied to explain some fracture phenomena at room temperature. Xiong et al. (2018) have investigated the fracture behavior of quenching and partitioning high-strength steels using flat uniaxial tensile specimens and double edge notched tension (DENT) specimens with a pre-crack. The phenomenon that void-dominated ductile fracture occurs in uniaxial tensile tests and brittle fracture occurs in pre-cracked configurations at room temperature can be interpreted with the proposed unified fracture criterion. This unified fracture criterion explains the phenomenon that cleavage fracture can occur after a significant amount of plastic deformation in some brittle materials under controlled loading conditions. On the other hand, for materials with good tensile ductility, cleavage fracture can also be triggered as long as sufficient strength and high local triaxiality are provided.

6. Conclusions

Tensile tests using different sample geometries, three-point bending tests using Charpy specimens, and fracture mechanics tests have been performed at –196 °C under quasi-static conditions to systematically investigate the fracture behavior of an X70 pipeline steel covering a wide range of stress states. Based on experimental and finite element simulation results, the following conclusions can be drawn.

- In addition to the increase of strength, the tensile ductility of the investigated X70 steel is significantly improved when the temperature decreases from room temperature to –196 °C.
- Significant plastic deformation occurs in tensile tests using different geometries at –196 °C, and macroscopic brittle fracture occurs in Charpy and fracture mechanics tests.
- At –196 °C, far below the ductile to brittle transition temperature of this bcc material, the transition of failure mechanisms from cleavage fracture to shear failure is observed with decreasing triaxiality. In stress states with moderate triaxiality, the coexistence of ductile and cleavage failure mechanisms is discovered.
- A unified fracture criterion is proposed to describe the observed fracture behavior, which considers the transition of failure mechanisms due to changes of stress states.
- Depending on the failure mechanisms of metallic materials with a bcc structure, the stress state space can be divided into three regimes according to the proposed unified fracture criterion. The threshold boundary corresponding to the transition of failure mechanisms is determined by the strain hardening capacity and the cleavage fracture strength as an indicator of crack propagation resistance, which is affected by temperature, strain rate, and microstructure.

CRediT authorship contribution statement

Fuhui Shen: Conceptualization, Investigation, Data curation, Validation, Writing – original draft, Visualization. **Sebastian Münstermann:** Resources, Writing – review & editing, Funding acquisition. **Junhe Lian:** Conceptualization, Methodology, Writing – review & editing, Supervision, Project administration.

Declaration of Competing Interest

The authors declare no conflict of interest for the publication of this paper.

Acknowledgments

thyssenkrupp Steel Europe AG is gratefully acknowledged for materials supply and financial support. Simulations were performed with computing resources granted by RWTH Aachen University under project rwth0241.

Appendix. : Determination of displacements corresponding to a given gage length

During tensile tests at RT, the crosshead displacements and displacements corresponding to a gage length (50 mm for SDB and 40 mm for other geometries) have been measured with the assistance of a high-speed optical camera. During tensile tests at –196 °C, the crosshead displacements have been measured. Since the identical specimen geometries have been used at both temperatures, the measured crosshead displacements at –196 °C have been converted into experimental displacements corresponding to a given gage length for each geometry.

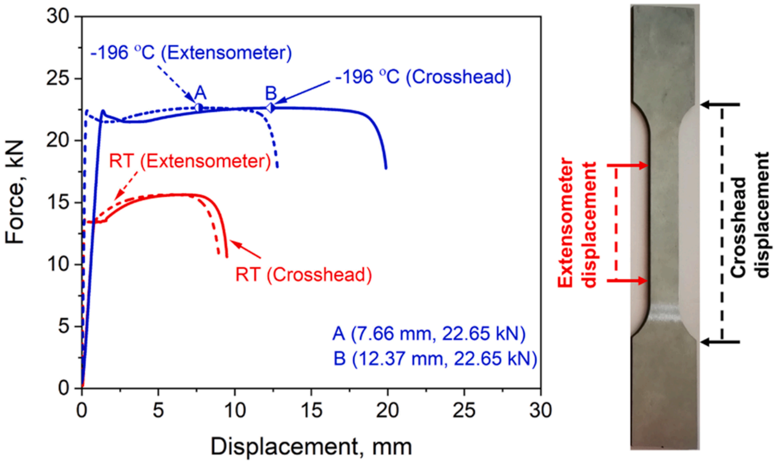

Fig A1. Determination of displacements corresponding to a given gage length based on measured crosshead displacements at –196 °C.

References

Anderson, T.L., 2017. Fracture mechanics: Fundamentals and Applications. CRC press.
Bai, Y., Wierzbicki, T., 2008. A new model of metal plasticity and fracture with pressure and Lode dependence. Int. J. Plast. 24, 1071–1096.
Bai, Y.L., Wierzbicki, T., 2010. Application of extended Mohr-Coulomb criterion to ductile fracture. Int. J. Fract. 161, 1–20.
Bao, Y., Wierzbicki, T., 2005. On the cut-off value of negative triaxiality for fracture. Eng. Fract. Mech. 72, 1049–1069.
Benzerga, A.A., Leblond, J.B., Needleman, A., Tvergaard, V., 2016. Ductile failure modeling. Int. J. Fract. 201, 29–80.
Beremin, F.M., 1983. A local criterion for cleavage fracture of a nuclear pressure vessel steel. Metall. Trans. A 14, 2277–2287.
Besson, J., 2009. Continuum models of ductile fracture: a review. Int. J. Damage Mech. 19, 3–52.
Boåsen, M., Stec, M., Efsing, P., Faleskog, J., 2019. A generalized probabilistic model for cleavage fracture with a length scale – influence of stress state and application to surface cracked experiments. Eng. Fract. Mech. 214, 590–608.
Brünig, M., Gerke, S., Schmidt, M., 2018. Damage and failure at negative stress triaxialities: experiments, modeling and numerical simulations. Int. J. Plast. 102, 70–82.
Chen, J., Cao, R., 2014. Micromechanism of Cleavage Fracture of metals: a Comprehensive Microphysical Model For Cleavage Cracking in Metals. Butterworth-Heinemann is an imprint of Elsevier.
Gao, X., Zhang, G., Srivatsan, T., 2006. A probabilistic model for prediction of cleavage fracture in the ductile-to-brittle transition region and the effect of temperature on model parameters. Mater. Sci. Eng. A 415, 264–272.
Gludovatz, B., Hohenwarter, A., Catoor, D., Chang, E.H., George, E.P., Ritchie, R.O., 2014. A fracture-resistant high-entropy alloy for cryogenic applications. Science 345, 1153–1158.
Ha, J., Baral, M., Korkolis, Y.P., 2019. Ductile fracture of an aluminum sheet under proportional loading. J. Mech. Phys. Solids 132, 103685. https://doi.org/10.1016/j.jmps.2019.103685.
Habib, S.A., Lloyd, J.T., Meredith, C.S., Khan, A.S., Schoenfeld, S.E., 2019. Fracture of an anisotropic rare-earth-containing magnesium alloy (ZEK100) at different stress states and strain rates: experiments and modeling. Int. J. Plast. 122, 285–318.
He, J., Lian, J., Golisch, G., Jie, X., Munstermann, S., 2017. A generalized Orowan model for cleavage fracture. Eng. Fract. Mech. 186, 105–118.
Hill, R., 1948. A theory of the yielding and plastic flow of anisotropic metals. Proc. R. Soc. A 193, 281–297.
Hu, Q., Li, X., Han, X., Chen, J., 2017. A new shear and tension based ductile fracture criterion: modeling and validation. Eur. J. Mech. A Solids 66, 370–386.
Khan, A.S., Liu, H.W., 2012a. A new approach for ductile fracture prediction on Al 2024-T351 alloy. Int. J. Plast. 35, 1–12.
Khan, A.S., Liu, H.W., 2012b. Strain rate and temperature dependent fracture criteria for isotropic and anisotropic metals. Int. J. Plast. 37, 1–15.
Kim, D.Y., Lee, M.G., Lee, C.A., Nguyen, N.T., Kim, H.Y., 2017. Failure prediction of AZ31B magnesium alloy sheet based on a micro-mechanical void model incorporating the asymmetric plasticity constitutive law. Int. J. Plast. 94, 98–121.
Kimura, Y., Inoue, T., Yin, F., Tsuzaki, K., 2008. Inverse temperature dependence of toughness in an ultrafine grain-structure steel. Science 320, 1057.
Knott, J., 2015. Brittle fracture in structural steels: perspectives at different size-scales. Philos. Trans. R. Soc. A 373, 20140126.
Lemaitre, J., 2012. A Course On Damage Mechanics. Springer Science & Business Media.
Li, F.F., Fang, G., 2022. Stress-state dependency of ductile fracture in an extruded magnesium alloy and its underlying mechanisms. Int. J. Plast. 152, 103258 https://doi.org/10.1016/j.ijplas.2022.103258.
Li, S., He, J., Gu, B., Zeng, D., Xia, Z.C., Zhao, Y., Lin, Z., 2018. Anisotropic fracture of advanced high strength steel sheets: experiment and theory. Int. J. Plast. 103, 95–118.
Lian, J., Sharaf, M., Archie, F., Münstermann, S., 2013. A hybrid approach for modelling of plasticity and failure behaviour of advanced high-strength steel sheets. Int. J. Damage Mech. 22, 188–218.
Lian, J., Shen, F., Jia, X., Ahn, D.C., Chae, D.C., Münstermann, S., Bleck, W., 2018. An evolving non-associated Hill48 plasticity model accounting for anisotropic hardening and r-value evolution and its application to forming limit prediction. Int. J. Solids Struct. 151, 20–44.
Lian, J., Wierzbicki, T., Zhu, J., Li, W., 2019. Prediction of shear crack formation of lithium-ion batteries under rod indentation: comparison of seven failure criteria. Eng. Fract. Mech. 217, 106520.
Lian, J., Wu, J., Muenstermann, S., 2015. Evaluation of the cold formability of high-strength low-alloy steel plates with the modified Bai-Wierzbicki damage model. Int. J. Damage Mech. 24, 383–417.
Lou, Y., Chen, L., Clausmeyer, T., Tekkaya, A.E., Yoon, J.W., 2017. Modeling of ductile fracture from shear to balanced biaxial tension for sheet metals. Int. J. Solids Struct. 112, 169–184.
Lou, Y., Yoon, J.W., 2017. Anisotropic ductile fracture criterion based on linear transformation. Int. J. Plast. 93, 3–25.
Lou, Y., Yoon, J.W., Huh, H., 2014. Modeling of shear ductile fracture considering a changeable cut-off value for stress triaxiality. Int. J. Plast. 54, 56–80.
Mohr, D., Marcadet, S.J., 2015. Micromechanically-motivated phenomenological Hosford–Coulomb model for predicting ductile fracture initiation at low stress triaxialities. Int. J. Solids Struct. 67-68, 40–55.
Mu, L., Jia, Z., Ma, Z., Shen, F., Sun, Y., Zang, Y., 2020. A theoretical prediction framework for the construction of a fracture forming limit curve accounting for fracture pattern transition. Int. J. Plast. 129, 102706.

Mu, L., Zang, Y., Wang, Y., Li, X.L., Araujo Stemler, P.M., 2018. Phenomenological uncoupled ductile fracture model considering different void deformation modes for sheet metal forming. Int. J. Mech. Sci. 141, 408–423.
Neimitz, A., Dzioba, I., 2015. The influence of the out-of- and in-plane constraint on fracture toughness of high strength steel in the ductile to brittle transition temperature range. Eng. Fract. Mech. 147, 431–448.
Orowan, E., 1949. Fracture and strength of solids. Rep. Prog. Phys. 12, 185–232.
Papasidero, J., Doquet, V., Mohr, D., 2015. Ductile fracture of aluminum 2024-T351 under proportional and non-proportional multi-axial loading: bao–wierzbicki results revisited. Int. J. Solids Struct. 69-70, 459–474.
Park, N., Huh, H., Lim, S.J., Lou, Y., Kang, Y.S., Seo, M.H., 2017. Fracture-based forming limit criteria for anisotropic materials in sheet metal forming. Int. J. Plast. 96, 1–35.
Park, N., Huh, H., Yoon, J.W., 2018. Anisotropic fracture forming limit diagram considering non-directionality of the equi-biaxial fracture strain. Int. J. Solids Struct. 151, 181–194.
Peng, Z., Zhao, H., Li, X., 2021. New ductile fracture model for fracture prediction ranging from negative to high stress triaxiality. Int. J. Plast. 145, 103057 https://doi.org/10.1016/j.ijplas.2021.103057.
Pineau, A., Benzerga, A.A., Pardoen, T., 2016. Failure of metals I: brittle and ductile fracture. Acta Mater. 107, 424–483.
Quach, H., Kim, J.J., Nguyen, D.T., Kim, Y.S., 2020. Uncoupled ductile fracture criterion considering secondary void band behaviors for failure prediction in sheet metal forming. Int. J. Mech. Sci. 169, 105297 https://doi.org/10.1016/j.ijmecsci.2019.105297.
Roth, C.C., Mohr, D., 2016. Ductile fracture experiments with locally proportional loading histories. Int. J. Plast. 79, 328–354.
Ruggieri, C., Dodds, R., 2017. A local approach to cleavage fracture modeling: an overview of progress and challenges for engineering applications. Eng. Fract. Mech. 187, 381–403.
Sathiyamoorthi, P., Moon, J., Bae, J.W., Asghari-Rad, P., Kim, H.S., 2019. Superior cryogenic tensile properties of ultrafine-grained CoCrNi medium-entropy alloy produced by high-pressure torsion and annealing. Scr. Mater. 163, 152–156.
Shen, F., Münstermann, S., Lian, J., 2020a. An evolving plasticity model considering anisotropy, thermal softening and dynamic strain aging. Int. J. Plast. 132, 102747.
Shen, F., Münstermann, S., Lian, J., 2020b. Investigation on the ductile fracture of high-strength pipeline steels using a partial anisotropic damage mechanics model. Eng. Fract. Mech. 227, 106900.
Shen, F., Wang, H., Liu, Z., Liu, W., Könemann, M., Yuan, G., Wang, G., Münstermann, S., Lian, J., 2022. Local formability of medium-Mn steel. J. Mater. Process. Technol. 299, 117368 https://doi.org/10.1016/j.jmatprotec.2021.117368.
Stoughton, T.B., 2002. A non-associated flow rule for sheet metal forming. Int. J. Plast. 18, 687–714.
Stoughton, T.B., Yoon, J.W., 2009. Anisotropic hardening and non-associated flow in proportional loading of sheet metals. Int. J. Plast. 25, 1777–1817.
Sun, S.J., Tian, Y.Z., An, X.H., Lin, H.R., Wang, J.W., Zhang, Z.F., 2018. Ultrahigh cryogenic strength and exceptional ductility in ultrafine-grained CoCrFeMnNi high-entropy alloy with fully recrystallized structure. Mater. Today Nano 4, 46–53.
Tekkaya, A.E., Bouchard, P.O., Bruschi, S., Tasan, C.C., 2020. Damage in metal forming. CIRP Ann. 69, 600–623.
Testa, G., Bonora, N., Ruggiero, A., Iannitti, G., Gentile, D., 2020. Stress triaxiality effect on cleavage fracture stress. Theor. Appl. Fract. Mech. 109, 102689.
Thomas, N., Basu, S., Benzerga, A.A., 2016. On fracture loci of ductile materials under non-proportional loading. Int. J. Mech. Sci. 117, 135–151.
Torki, M.E., Keralavarma, S.M., Benzerga, A.A., 2021. An analysis of Lode effects in ductile failure. J. Mech. Phys. Solids 153, 104468.
Wang, Y.M., Ma, E., Valiev, R.Z., Zhu, Y.T., 2004. Tough nanostructured metals at cryogenic temperatures. Adv. Mater. 16, 328–331.
Xiong, Z., Jacques, P.J., Perlade, A., Pardoen, T., 2018. Ductile and intergranular brittle fracture in a two-step quenching and partitioning steel. Scr. Mater. 157, 6–9.
Xue, L., 2007. Damage accumulation and fracture initiation in uncracked ductile solids subject to triaxial loading. Int. J. Solids Struct. 44, 5163–5181.
Xue, L., Wierzbicki, T., 2008. Ductile fracture initiation and propagation modeling using damage plasticity theory. Eng. Fract. Mech. 75, 3276–3293.
Zhang, Z., Wu, Y., Huang, F., 2022. Extension of a shear-controlled ductile fracture criterion by considering the necking coalescence of voids. Int. J. Solids Struct. 236-237, 111324 https://doi.org/10.1016/j.ijsolstr.2021.111324.